Compositional analysis of laser welds in a $Cu_{46.5}Zr_{46.5}A_7$ glass forming alloy

Harrison Tyler Holberton

Georgia Institute of Technology

Undergraduate Research Thesis

December 14, 2021

Dr. Aaron Stebner – Mentor

Dr. Mary Lynn Realff – Second Reader

Abstract

Laser additive manufacturing is a promising manufacturing method of bulk metallic glasses. Study and understanding of the heat affected zone and fusion zones are crucial in developing this manufacturing technique. A cast $Cu_{46.5}Zr_{46.5}A_7$ sample was processed at laser powers and scan speeds varying from 75-370W and 100-900 mm/s respectively to determine the effects of processing parameters on weld composition for use in additive manufacturing. Copper content was found to generally decrease through the weld fusion zone, and increase through the heat affected zone. Zinc was unexpectedly present in analysis. Cracking occurred at significantly different linear energy densities and appeared to correlate more strongly with laser power at these parameters, supporting previous research that using energy density alone to predict additive manufacturing processes.

Introduction

The field of material science and engineering is as old as technology itself. Formally synthesized and separated from previous disciplines in the 1960's, material scientists and engineers first synthesized the class of materials known as amorphous metals (aka metallic glasses or amorphous alloys) shortly after the formal inception of the field (Junwei, 2016). Metallic glasses are complex metal alloy systems that are cooled extraordinarily quickly. The atoms do not have time to arrange themselves in an ordered manner that is characteristic of conventional metal structures. The composition of these metal systems directly affects the critical cooling rate, as the composition is directly related to the kinetics of crystallization, and thermodynamic favorability of carbides, material phases, nucleated inclusions, and phase transformations involved during material cooling. (Trexler and Thadhani, 2010) If the molten material is cooled more quickly than the kinetics of crystallization which can occur, the structure that is formed is amorphous, possessing no ordered short-range or long-range order. This amorphous nature of the metal system is thus an amorphous metal, the structure of which gives rise to its characteristic hardness, toughness, wear and corrosion resistance. (Trexler and Thadhani, 2010) These properties are uniquely placed between conventional glasses/ceramics and metals, due to the presence of metallic bonds found in metals and the glassy structure of the bulk material.

The discovery through synthesis of amorphous alloys by Duwez and his colleagues in 1960 yielded a novel class of material with immense amounts of technological potential. As a structure which combines metallic bonds with an amorphous structure, which results in a unique combination of properties compared to either metals or glasses. The initial alloy system was a 25at% Si-Au, and a flake 10μm thick was found to have an amorphous structure which was identified through X-Ray diffraction. Initial synthesis of these types of alloys required massive amounts of heat transfer, and at least 1 dimension was incredibly limited. Due to this, initial processing methods were only able to produce thin foil samples. This first system was incredibly unstable, and impurities were found in the same specimen 24 hours after synthesis. In the decades afterwards, more stable and complex alloy compositions have been developed and

characterized. Once developed to a point where they could be manufactured in bulk, the class of materials became known as bulk metallic glasses. The advent of bulk metallic glasses allowed the bulk properties of this material, which are crucial to practical engineering applications, to be discovered and studied. Compositions which could be cast into bulk dimensions were developed with the formation of 4-fold and 5-fold compositions, and allowed for BMG's to be used in commercial applications.

Despite these developments, however, the dimensional limitations remain through conventional manufacturing techniques. Due to the large heat transfer requirements, the materials are limited in at least one dimension, resulting in the bulk form of metallic glasses existing as foils, thin plates, or wires and these bulk forms are limited in their structural applications. Additive manufacturing is a process which has the potential to overcome these limitations, due to the small amount of material which is worked at any instantaneous point in time. During additive manufacturing of metals, a powdered form of the metal is heated and thinly deposited onto a substrate, and cool into a thin layer. The process repeats, and as additional layers are added, the geometry of the final product takes shape. During fusion of the next layer, heat spreads through material which has already been deposited and has the potential to deleteriously affect the morphology of the alloy.

The favorability of metallic glass formation is dependent on several conditions. First, the metal must be a multicomponent alloy, ideally with large or complex crystal unit cells and a large amount of entropy in the super-cooled phase. This creates an energy barrier at the solid-liquid transformation which must be overcome for crystallization to occur. Additionally, the components must have a large radius mismatch between components. This radius mismatch increases the packing density of the material in both solid and liquid phase, as well as the required volume change during crystallization. This required volume change of crystallization also works in conjunction with complex crystal unit cells to further increase the energy barrier of the solid-liquid transformation. Further, the components must have a negative heat of mixing, which increases the solid-liquid energy barrier, and slows the nucleation rate during cooling. This third factor increases the favorability of an amorphous phase thermodynamically, and slows the kinetics of crystallization down which allows for a slower critical rate of cooling for glass formation to occur. Lastly, the composition should be at or near a deep eutectic phase, as the liquid to solid phase change of a eutectic material is extraordinarily rapid.

Though it has been 60 years since the discovery of this class of materials, there remains limitations to be overcome for this material in current commercial applications due to difficulties in manufacturing bulk samples due to economic and engineering constraints. The economic feasibility is difficult but not impossible to overcome utilizing conventional manufacturing techniques due to the extensive processing of materials that is required before they can be made into workable samples. (Trexler and Thadhani, 2010) Additional manufacturing constraints are heavily bounded by heat transfer mechanics. The first sample of this material class, only 10 micrometers in thickness, was obtained through cooling rates on the order of 10^5-10^6 K/s. (Cheng, 2010); more recent quaternary systems have been discovered with cooling rates on the order of 250 K/s. (Lin and Johnson, 1998), while these developments do make manufacturing in

bulk easier, they also bring the focus of this research project: Production of bulk samples through laser additive manufacturing, further into the realm of commercial feasibility. For this area of research and production to progress, known parameters must be established for alloy systems of interest. For this experiment, a $Cu_{46.5}Zr_{46.5}A_7$ sample was studied.

Literature Review

The advantages of applying additive manufacturing techniques in the manufacturing of metallic glass products specifically addresses the primary difficulty of manufacturing these materials in bulk: critical cooling rate. Due to the limitations imposed by critical cooling rates in manufacturing, samples of metallic glasses are limited dimensionally, as one dimension must be small enough in relation to the others to maximize surface area to volume ratio, utilized by Klement in 1960, as well as a rather exotic method of ultrasonic additive manufacturing utilized by Wu et. al. in 2019. This approach is also taken advantage of in vapor deposition, where the metal system is vaporized and deposited on a substrate (Trexler and Thadhani, 2010). Other manufacturing techniques have been utilized whereas one or two dimensions must be significantly smaller than the third as utilized by Lieberman in 1976 in a process referred to as melt spinning. Melt spinning, where a small amount of sample is continuously deposited onto a cooled spinning disk (Lin and Johnson, 1998), direct laser deposition, powder bed fusion, and directed energy deposition, where the metal system is in powdered form and sintered using lasers (Li, 2017) are the more conventional methods utilized to bulk manufacture metallic glasses. With regards to additive manufacturing, technologies not utilizing pure powder-based feedstock have emerged. These technologies are: wire, molten liquid, ribbon, shot, and metal powder infused with polymer binders. Additional methodologies developed that can be utilized for industrial fabrication include manufacturing from sheet-stock, polymer-bound powders, or ultrasonic additive manufacturing. Each of these additional methodologies take advantage of limiting one or more dimensions relative to the other, and alloying for rapid heat transfer out of the material during cooling. (Bordeenithikasem et al., 2017, 2018)(Wu et al. 2019)

Current research is returning to a more conventional powder-based process utilizing laser additive manufacturing techniques (Bordeenithikasem 2020) (Hofmann 2018). Forms of laser depositions are viewed favorably in amorphous structure materials due to the aforementioned tertiary and quaternary alloy systems which require slower cooling rates, which can be achieved through relatively small melt pools to overall sample size which is characteristic in LAM. These lower cooling rates and small melt pools in processing allow larger dimensioned samples to be produced. The various processes included in Laser Additive Manufacturing rely on depositing metal powder onto the bed of the apparatus in layers. A laser is then passed over the powder, melting it. Once all the material for the current layer has been melted, another layer of powder is deposited and the process repeats until the final product is manufactured. Various parameters are controllable and include laser speed (how quickly the laser moves across the surface of the powder), laser power, and spot size in some models of printers. A difficult question to answer regarding these parameters is “How does scan rate and scan speed affect the cooling and morphology during processing?” While there is the opinion that a simple volumetric energy density formula can be manipulated to answer this, Bertoli disagrees due to his findings that

“[Volumetric Energy Density] fails to capture melt pool physics, hence it poorly predicts both melting condition and track morphology.”(Bertoli, 2016). Selective laser melting, as used by Bertoli in his paper, serves as an umbrella term covering all technologies relying on laser melting in additive manufacturing.

During conventional processing through additive manufacturing, energy applied to the material spreads further through the material than the fusion zone due to heat transfer in what is known as the heat affected zone (HAZ), which varies with the amount of energy applied to the material. While the effects are conventionally studied in welding, this mechanism can apply to any processing which heats the material above a morphologic transformation temperature. In low alloy steels, during welding, the HAZ has been shown to decrease mechanical strength, and deleteriously affect the performance of the material. Additional heat treatment was required to return the material properties to desired levels. (Mohandas et al. 1999) This mechanism is prevalent in additive manufacturing of metals, as material which has been deposited and fused in a layer is subsequently reheated as additional layers are fused and the applied energy spreads through the material. Understanding the HAZ morphology is crucial for the success of additively manufacturing pure BMG products.

Most BMG additive manufacturing studies focus on processing parameters for obtaining dense parts utilizing alloy powders for metal systems which have been studied and for which data has been made available through single-track experiments. In a single-track experiment, non-overlapping melt pools are created with unique processing parameters, and the morphology each studied. From these experiments, parameter envelopes can be selected for and later established through additive manufacturing experiments.

Methodology

The sample was ground and polished to a uniform surface finish of 0.5 micron to remove surface oxides, provide a uniform surface finish, and ensure no surface imperfections would interfere with laser absorption. The samples were then sandblasted with a 100/140 mesh grit equivalent glass beads to provide a final uniformly matte finish across the surface of the sample to increase absorptivity from the prior mirror finish. Samples were then scanned in an EOS INT M280 printer with the following parameters displayed below in Table 1. These parameters were selected to encompass a large parameter envelope, both within and outside of established values for an amorphous morphology obtained through prior literature.

Table 1 shows the track number with corresponding laser power and scan speed for that respective track

Track (#)	Power (W)	Scan Speed (mm/s)		Track (#)	Power (W)	Scan Speed (mm/s)
1	75	100		14	225	700
2	75	300		15	225	900
3	75	500		16	300	100
4	75	700		17	300	300
5	75	900		18	300	500
6	150	100		19	300	700

7	150	300		20	300	900
8	150	500		21	370	100
9	150	700		22	370	300
10	150	900		23	370	500
11	225	100		24	370	700
12	225	300		25	370	900
13	225	500				

Note that the maximum limitations of the EOS INT M280 for laser power and scan speed are 400W and 7000 mm/s respectively. The experimental parameter ranges in the table below hypothesized to be the ideal range of various BMG's based on previous literature shown below in Table 2. (Li et al. 2016) (Ouyang et al., 2017)

Table 2 shows processing parameters for glass forming alloys which have formed amorphous structures in previous literature.

Alloy	Laser Power Range (W)	Laser Speed (mm/s)
Zr-Based	150-300	500-2500
Cu-Based	100-400	500-2500
Ni-Based	200-400	200-2000

25 Individual tracks were melted on the sample in a radial pattern, shown below in Figure 1 (left). These samples were then wire EDM cut through the centers of the tracks, shown below in Figure 1 (right), and polished to a 0.3µm finish. The first and last tracks are numbered in Figure 1 (left).

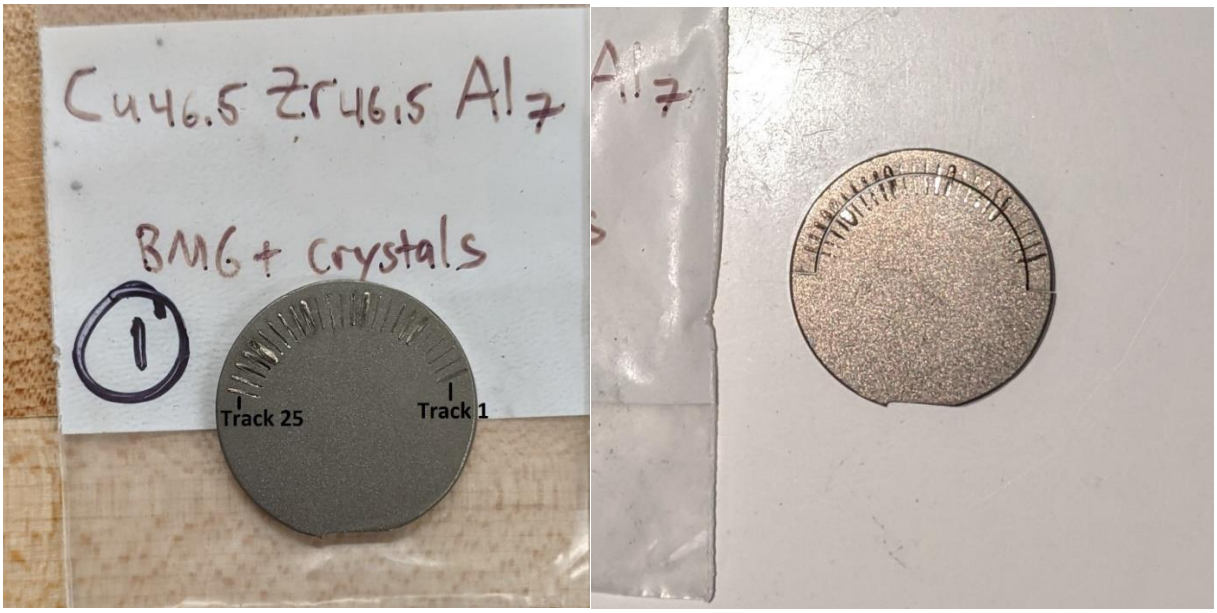

Figure 1 shows the sample after track welding (left) and after wire EDM cutting and cross section polishing (right)

Images of both the surface and cross sections of the melt pool were taken with a Phenom XL G2 SEM, with elemental analysis performed with an Axia ChemiSEM.

Results

The results are divided into low, moderate, and high laser power. Low laser power includes parameters below the processing envelope for similar alloys established in literature. Moderate laser power includes parameters which are in the processing envelope for similar alloys established in literature. High laser power includes parameters which are above the processing envelope for similar alloys established in literature.

All graph figures below are shown as distance from the surface on the x-axis with the exception of the base material. Quantitative maps of SEM images are provided where available. Some weld tracks do not have quantitative maps due to errors in data collection. Colors shown in the quantitative map correspond to the element colors in the graph immediately below within each figure, with element percentages shown in atomic percent. The surface, point 1, of each graph begins at the y-axis of the graph.

Zinc was included in the analysis despite not being present within the material due to its unexpected detection in two separate SEMs during data collection.

Base Material

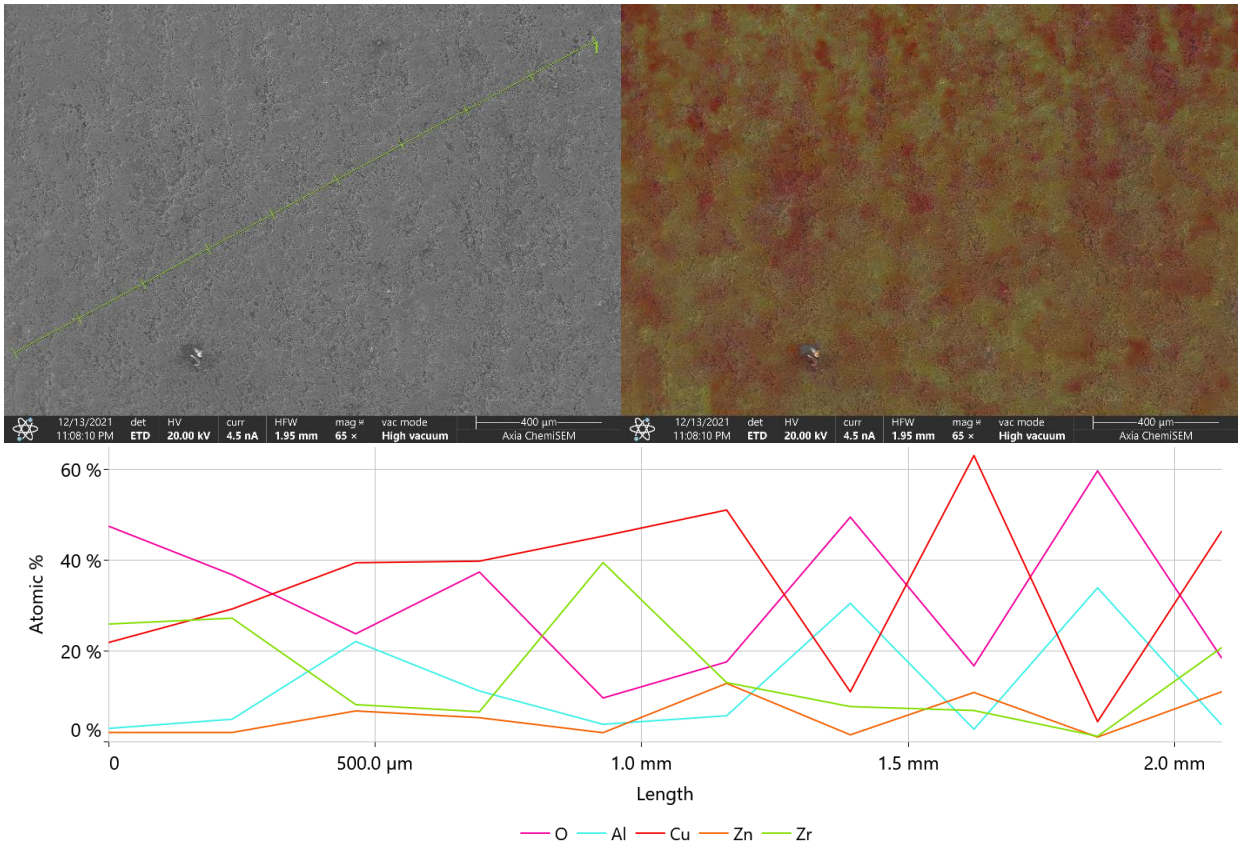

Figure 2 shows SEM imagery of the base material with line analysis (top left) and quantitative map of the same (top right). Points taken along the line are shown as cross hatches along the line. The corresponding graph (bottom) shows the corresponding elements present at each point along the line. Note the large variance in elements present (differences in

coloration and values for each element) within the base material, and that the light and dark regions in the SEM image does not correlate with compositional changes.

Within the base material there is a large variance in the ratio of Cu and Zr at different points within the material. An apparent trend is an inverse relationship between copper and oxygen from oxides within the material. Additionally, there appears to be a weak direct relationship between copper and zinc throughout the material. SEM imagery of the base material shows a dark porous phase throughout the unprocessed material.

Low Power, Tracks 1-5

Track 1

Figure 3 below shows an OM image (top left) and SEM image (top right) of the weld surface. It also shows an SEM image (middle left) and corresponding quantitative map of elements present (middle right) of the weld cross section. A corresponding graph of and Immediately apparent within the OM image is that the weld pool does not appear to be continuous, which is confirmed through the imperfections seen in across the surface which appear as craters. Cross sectional images shown in the middle of the figure above do not show a readily visible fusion zone or HAZ. The behavior of these zones is inferred through the microscopic feature which the analysis line runs through. Point 3, at approximately 100µm in Figure 1 (bottom) is the boundary of the melt pool. Within the fusion zone there is a significant decrease in copper from the surface to the boundary of the HAZ. Within the HAZ, copper content increases and varies similarly to the bulk material, shown at 400-450µm, with no discernable compositional or trend change between the HAZ and the bulk material.

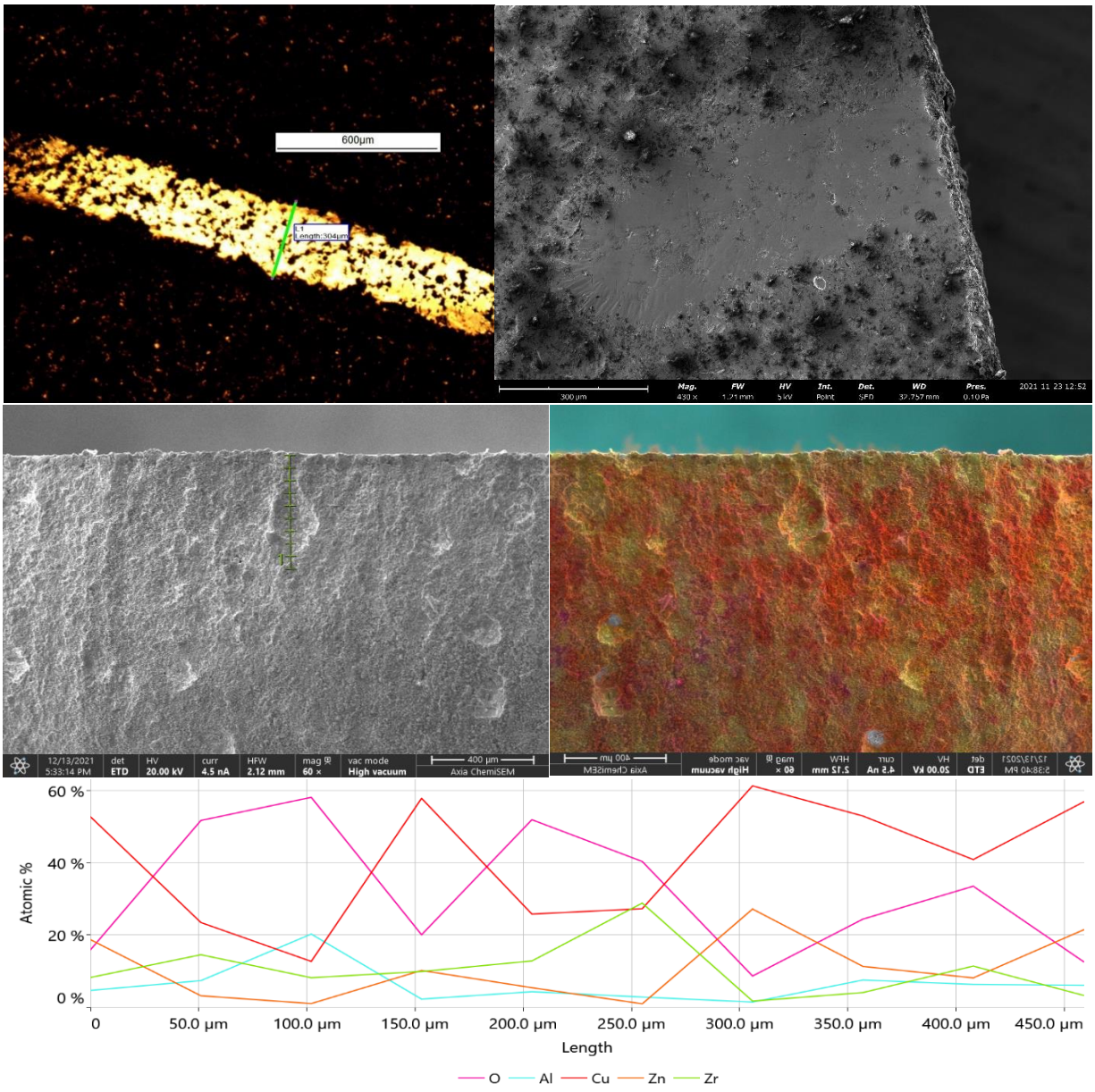

Figure 3 shows an OM image of the surface of the track (top left), SEM image of the cross section of track 1 with the line analysis through the weld marked in green (left), and the quantitative element map of the same (right). Note the bulbous feature which the line analysis cuts through, with the edge of this feature centered with the weld at the surface.

Track 2

Figure 4 below contains the data gathered for track 2. From OM (Top Left), track 2 appears to be smooth and mostly continuous which is confirmed through the SEM image of the weld surface (Top Right). Line analysis is shown in the center image. A similar microscopic feature as in Figure 1 is apparent, and was used to infer the weld pool and HAZ. Points 1 and 2 in the graph (bottom) show a significant increase in copper content within the weld pool. The boundary between the weld pool and HAZ appears to be between points 2 and 3 (50-100µm), which the amount of copper present remaining steady across the transition zone. Within the HAZ the copper content decreases then increases as distance from the surface increases. Additionally, the

content of zinc is inverse with the copper content within this region. The end of the HAZ appears to be around point 7 (~310 µm), with a sharp decrease in copper content, and increase in oxygen. A quantitative map is not available for track 2.

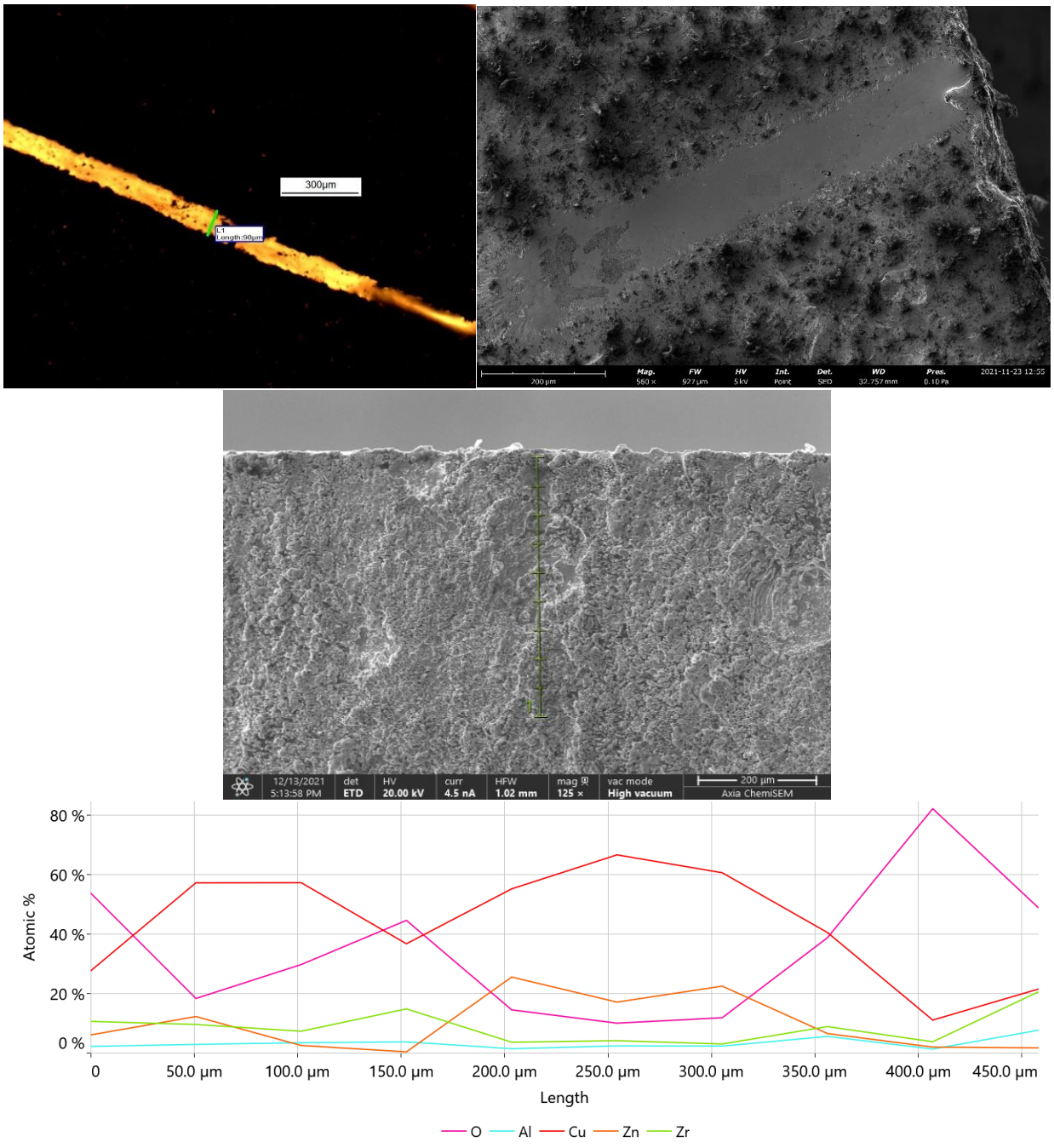

Figure 4 shows an OM image (top left) and SEM image (top right) of the weld surface, note that it is much more continuous and smoother in appearance. Line analysis is shown (center), with the compositional data from each point shown in the graph (bottom) is also shown

Track 3

Figure 5 below shows OM and SEM of the weld surface, SEM and a quantitative map of the weld cross section, and element composition. From OM and SEM of the surface, the weld is continuous and smooth. The melt pool (point 1), appearing as yellow in the quantitative map, appears to be equiatomic CuZr, a line compound in the binary Cu-Zr phase diagram. The melt pool and HAZ are rich in Zr. The amount of copper present increases with distance from the weld surface through the fusion zone (points 1-3, 0-100µm), decreases then increases through the HAZ (4-6, 150-250µm). The transition from the HAZ to the bulk material (point 7, 300µm) is marked with a sharp decrease in Zr, and increase in Cu. The bulk material (point 8-10, 350-450µm) show

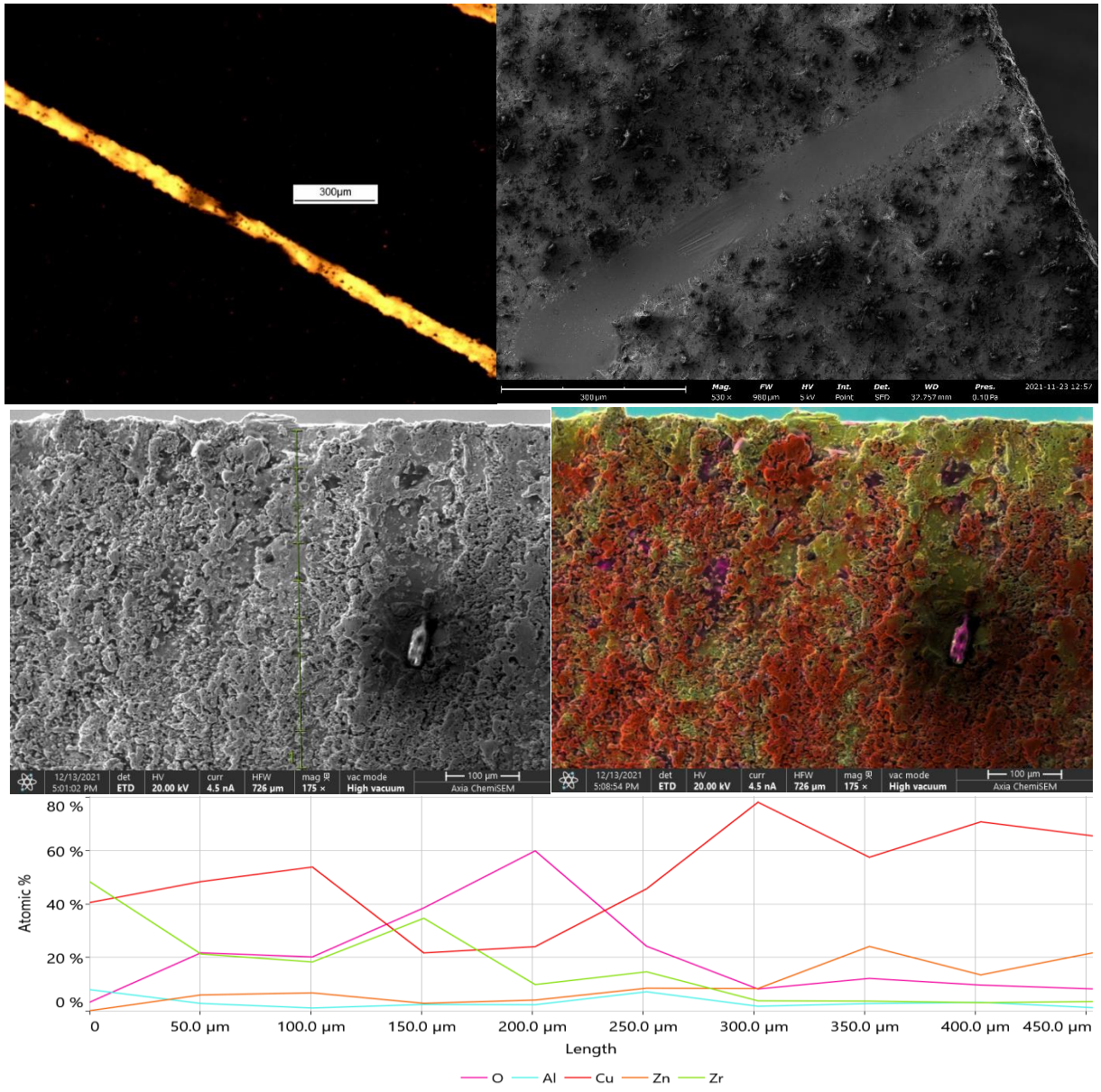

Figure 5 shows OM (top left) and SEM (top right) of the weld surface. SEM imagery (center left) and a quantitative map (center right) of the weld cross section is also shown, with element compositions shown in the graph (bottom).

Track 4

Figure 6 below shows OM and SEM imagery of the weld surface, SEM imagery and a quantitative element map of the weld cross section, and graphs showing atomic percent composition both through the weld and across the weld is bordered by two equiatomic CuZr regions. It is difficult to separate the melt pool from the HAZ due to the layered compositions, however it appears the melt pool extends from the surface to point 3 (0 - 100µm) with the heat affected zone unable to be differentiated from the bulk material through compositional analysis alone due to extraordinarily large variance in all elements past point 3 (100µm). The boundary of the weld is clear through the compositional analysis across the weld, primarily through the change in Zr content through 15at% as the weld boundary is crossed. (~75µm, ~375 µm)

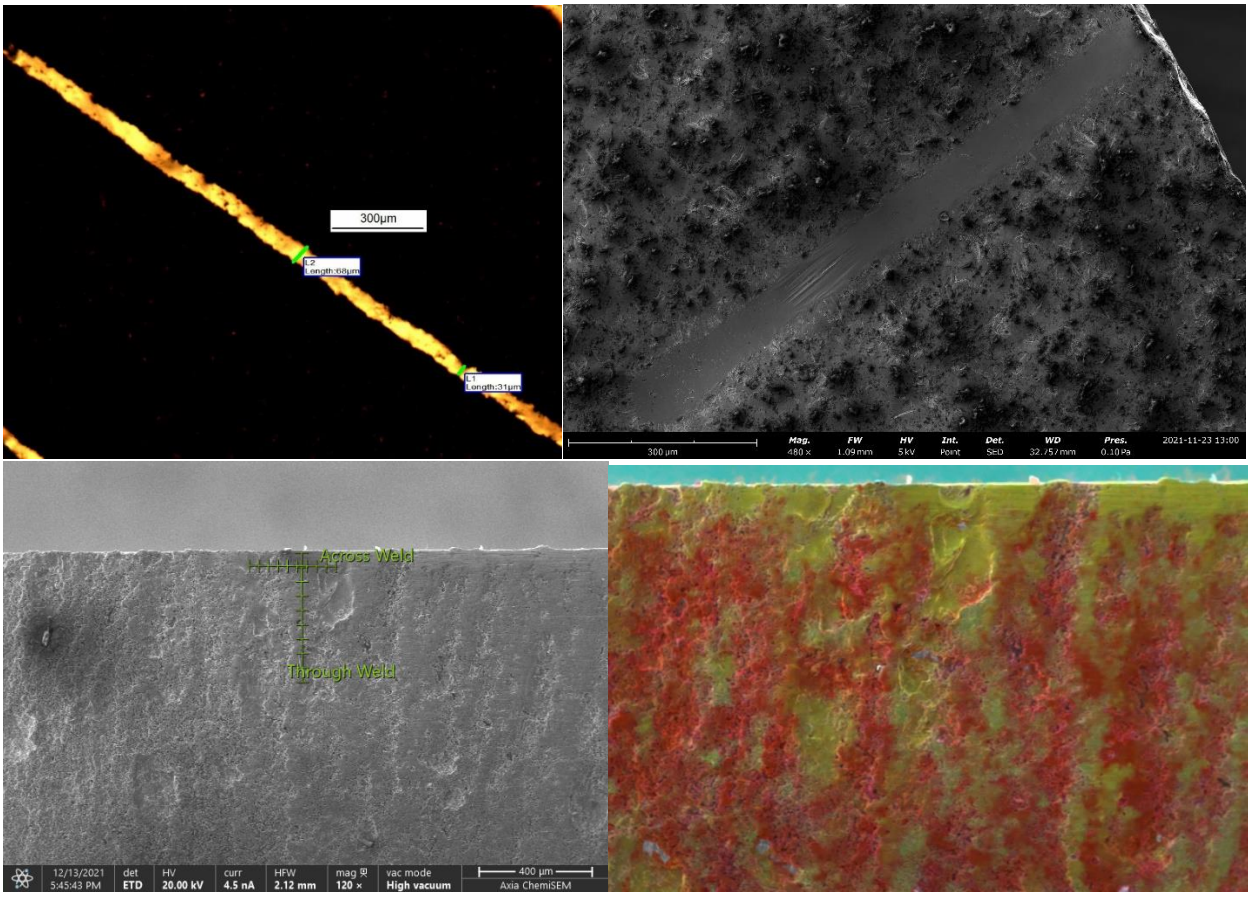

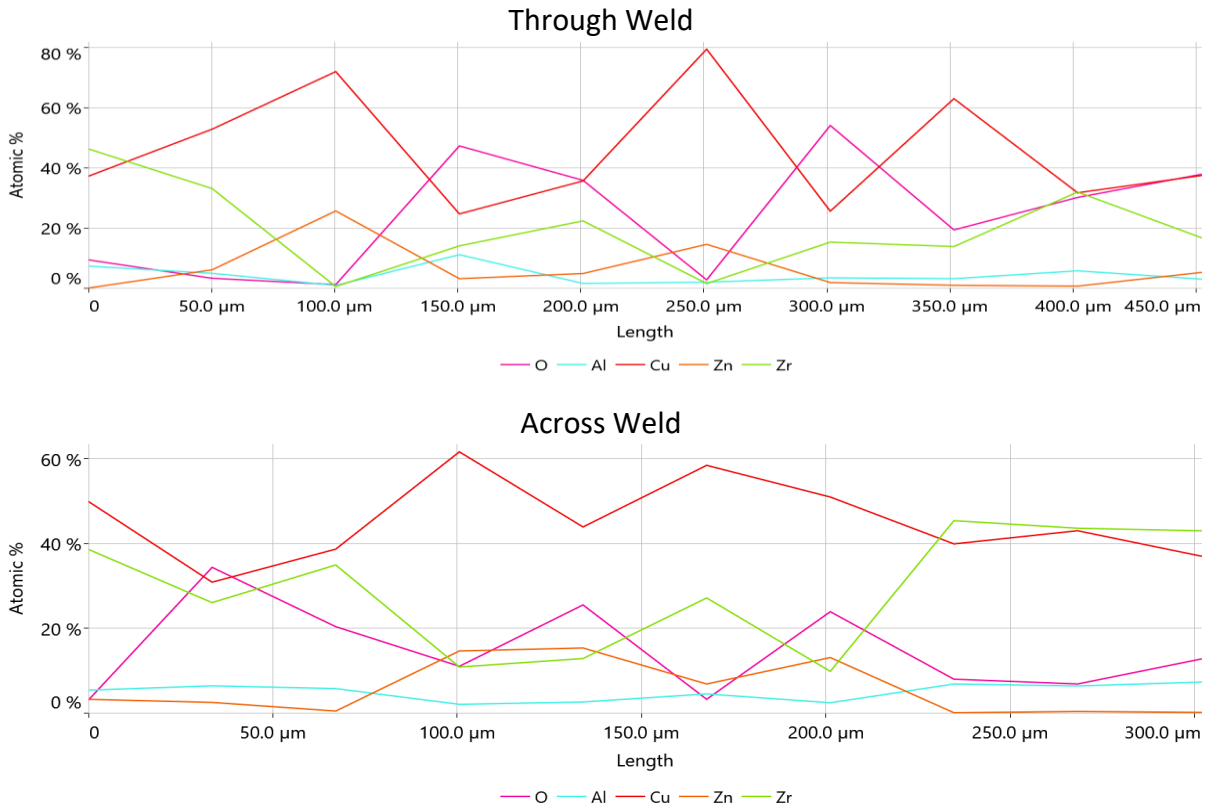

Figure 6 shows OM (top left) and SEM imagery of the weld surface, SEM (center left) and a quantitative map(center right) of the weld cross section. The top graph shows the elemental composition of the weld moving away from the surface, with the bottom graph showing the composition across the weld pool, left to right.

Track 5

Figure 8 below shows OM and SEM imagery of the weld surface, as well as SEM imagery and compositional analysis of the cross section. The lack of a quantitative map makes discerning the composition of the track through the various zones. However, an additional compounding factor has likely made meaningful composition analysis of this track impossible. Figure 7 below is the quantitative map of the previous track. Note the yellow, equiatomic CuZr phase shown in the top right. This continues throughout the rest of the sample and is a likely source of error due to processing. From the OM and SEM of the weld surface, it is smooth and continuous. Cracking is visible in the SEM image of the weld cross section to the left of the second point, likely due to crystallization shrinkage.

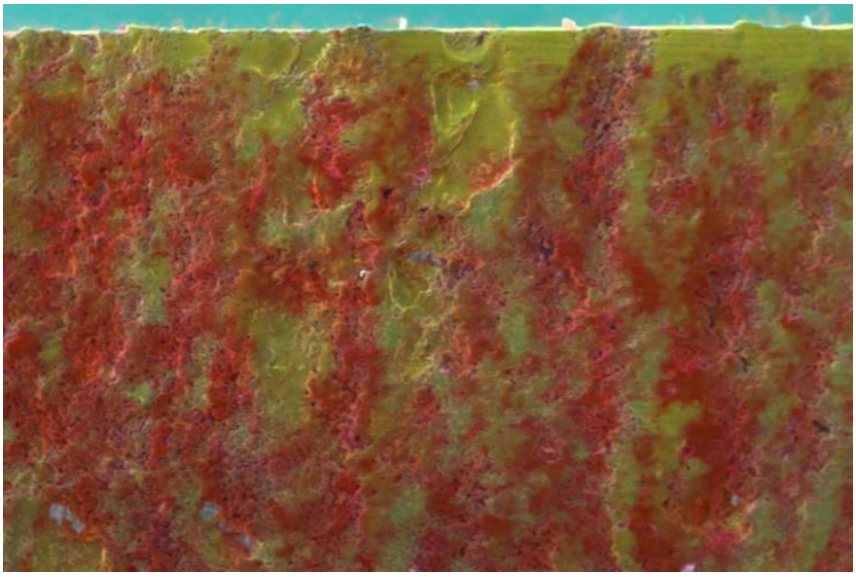

Figure 7 shows a continuous yellow phase along the surface in the top right of the image

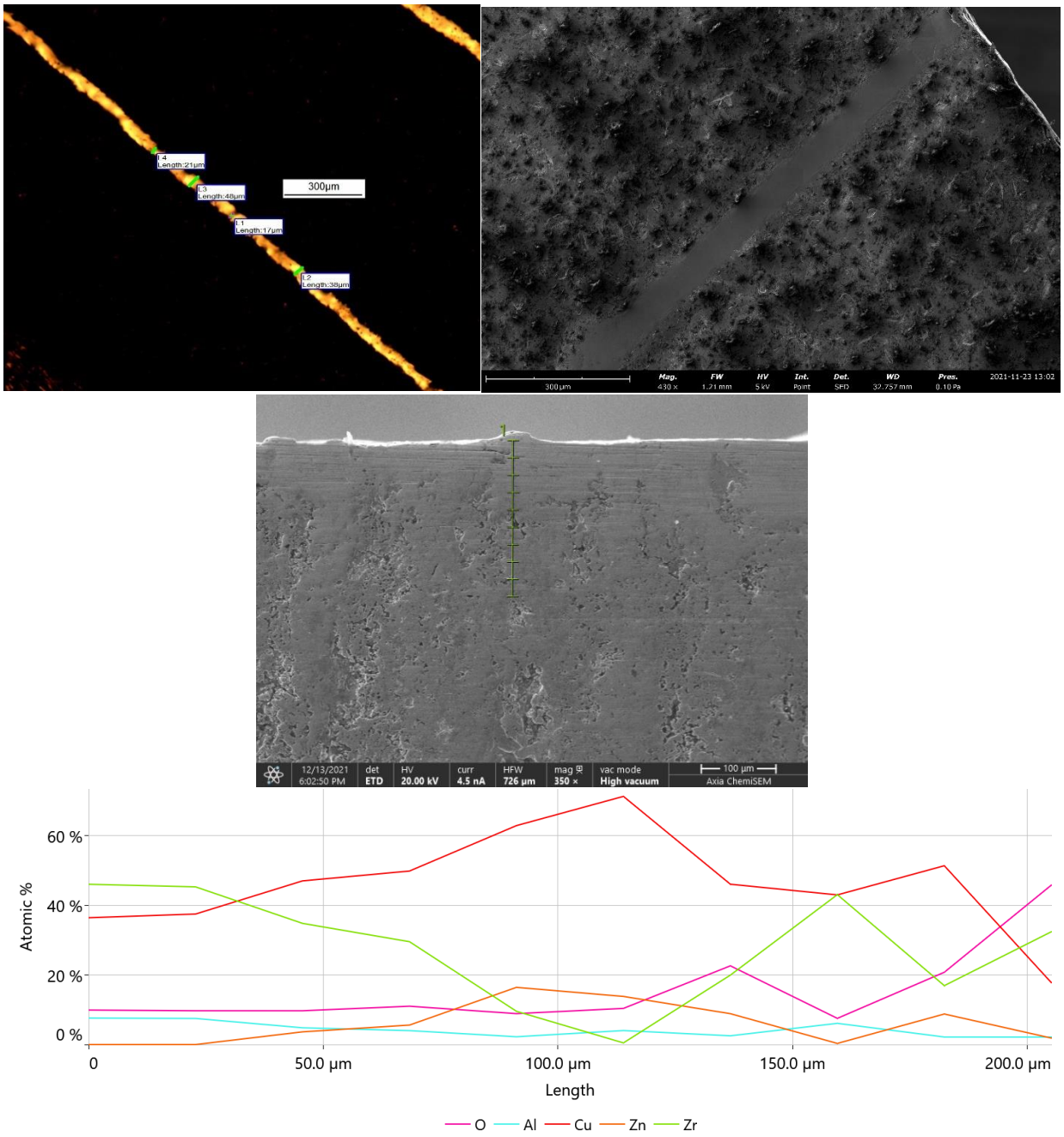

Figure 8 shows OM (top left) and SEM (top right) imagery of the weld surface, as well as SEM imagery (center) and compositional analysis (bottom) of the weld. Note that the surface of this track through (~75 µm) is entirely equiatomic CuZr

Moderate Power – Tracks 6-20

Track 6

Figure 9 below shows a continuous but extraordinarily rough weld surface, which is confirmed through the corresponding SEM imagery, and is likely to be crystalline. Compositionally, there is a relatively Zr-rich melt pool from the surface to 100 µm. The composition of the HAZ varies across the melt pool rather than through the melt pool, with Zr-rich fibrils extending along the

weld shown as continuous yellow regions extending from the surface of the sample in this region. The light phase show in the SEM image of the cross section shows correlation with the Zr-Rich phase, shown as yellow on the quantitative map. Bulk material appears to begin between 600-650 µm from the surface.

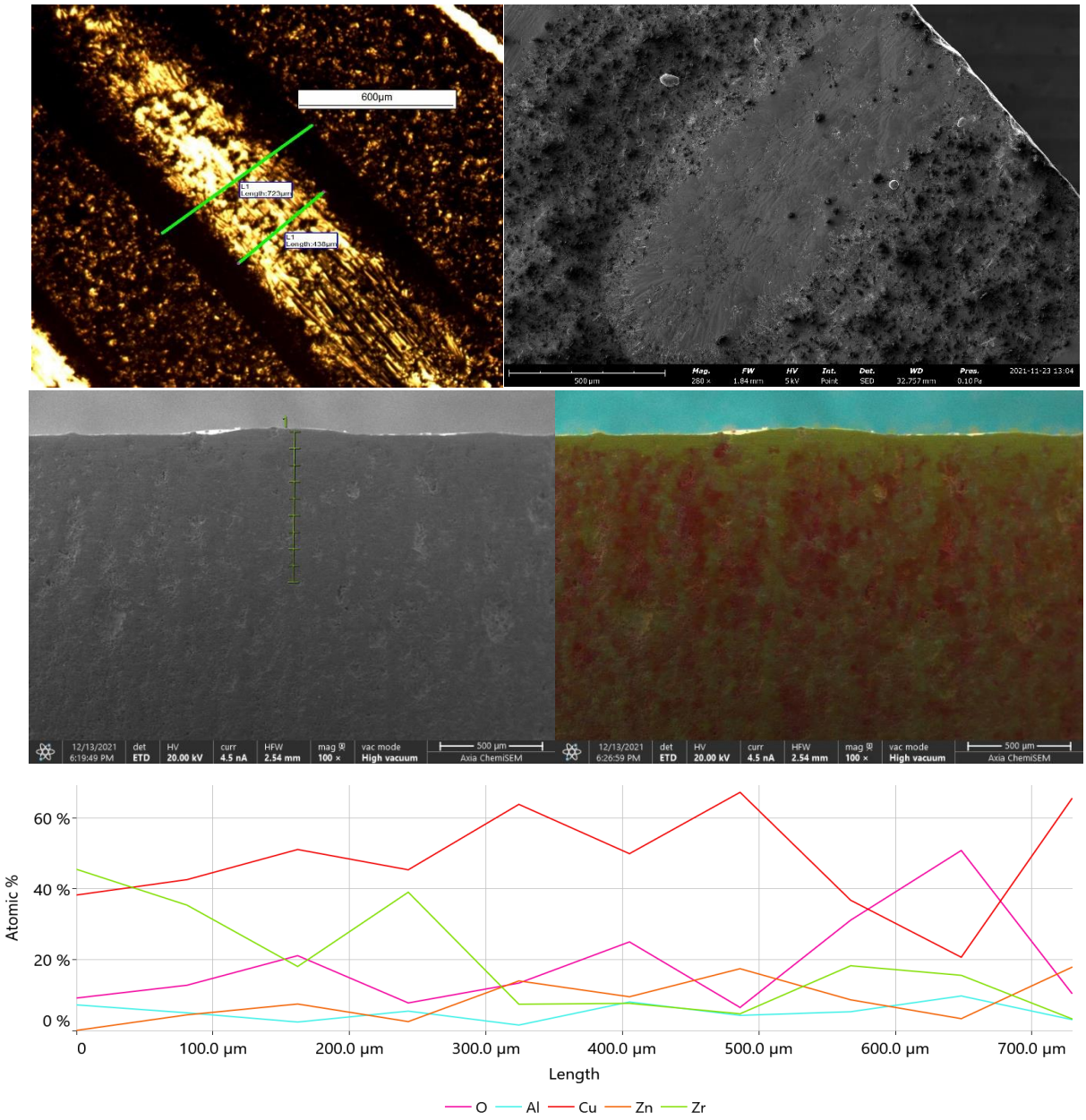

Figure 9 shows OM (top left) and SEM (top right) imagery of the weld surface, SEM imagery (center left) and a quantitative element map (center right) of the weld cross section. Compositional analysis is shown in the bottom graph.

Track 7

Figure 10 below shows OM and SEM imagery of the weld surface, and SEM imagery of the weld cross section. A quantitative map of this track unavailable, but weld can be seen in the rightmost quarter of Figure 9 (center right). OM and SEM of this track show a rough surface with volumetric shrinkage.

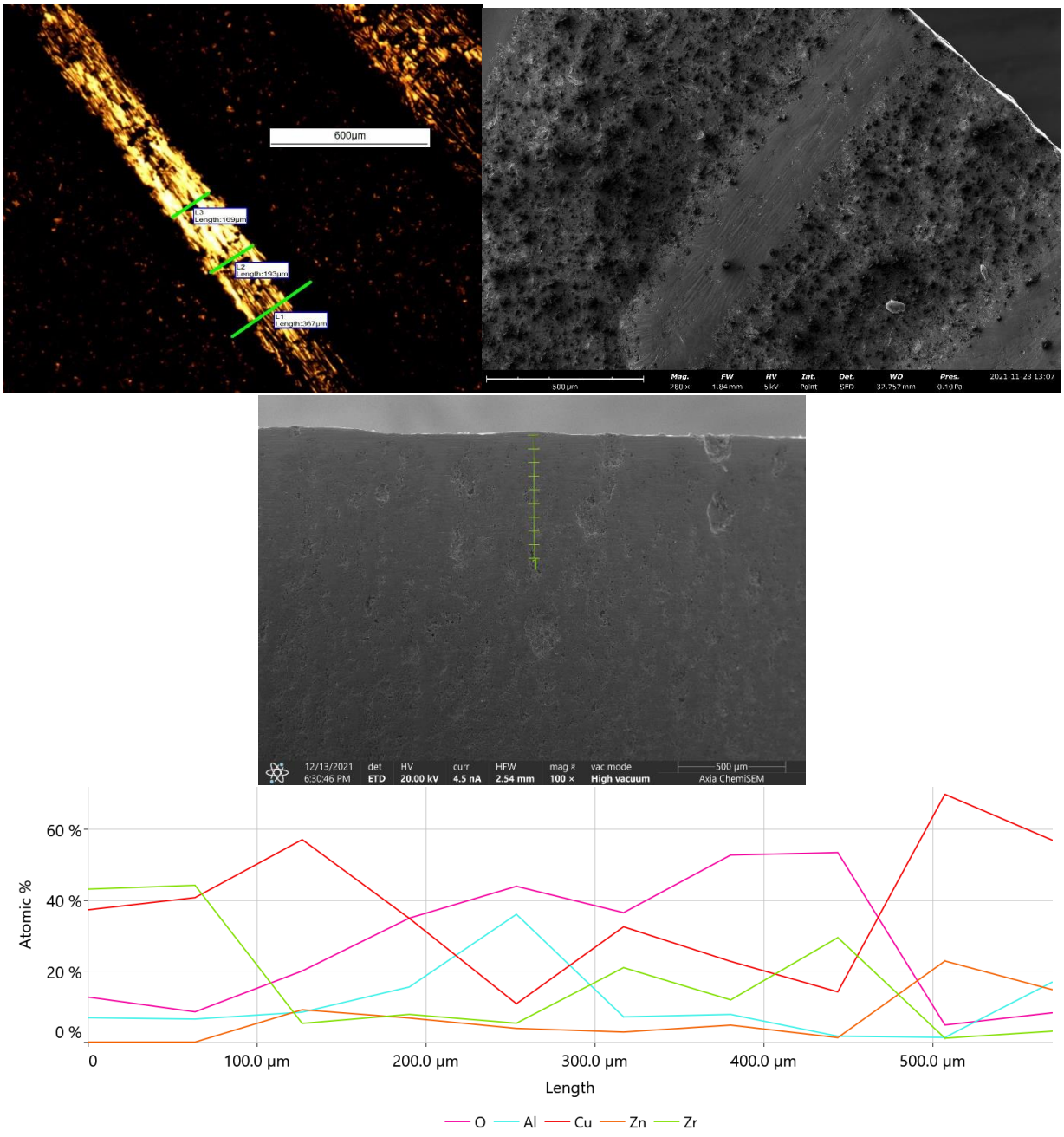

Figure 10 shows OM (top left) and SEM (top right) imagery of the weld surface, SEM imagery (center left) and a quantitative element map (center right) of the weld cross section. Compositional analysis is shown in the bottom graph.

Track 8

Figure 11 below shows OM and SEM imagery of the weld surface, SEM imagery and a quantitative map of the weld cross section, and compositional analysis of the weld. OM imagery shows a smooth but discontinuous melt pool, with craters visible in SEM imagery of the weld surface. There does not appear to be any shrinkage or physical texturing due to volume change. SEM imagery of the weld cross section (center left) shows the light phase in much better contrast, and shows a clear correlation with the relatively Zr-rich phase shown in yellow in the quantitative map.

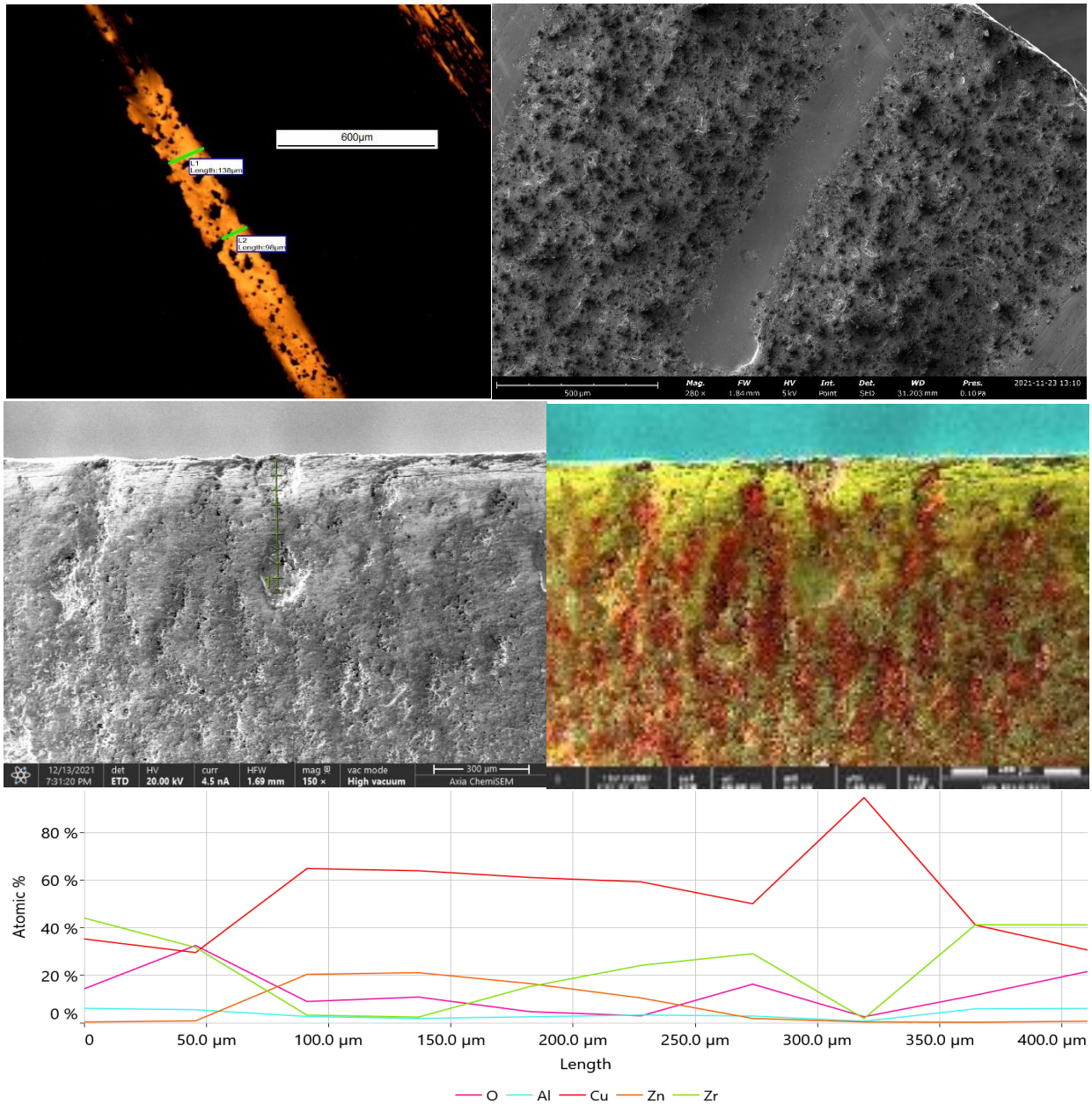

Figure 11 shows OM (top left) and SEM (top right) imagery of the weld surface, SEM imagery (center left) and a quantitative element map (center right) of the weld cross section. Compositional analysis is shown in the bottom graph.

Track 9

Figure 12 below shows OM and SEM imagery of the weld surface, SEM imagery and a quantitative map of the weld cross section, and compositional analysis of the weld. OM shows what appears to be a discontinuous phase. This is not correlated with the SEM image of the weld pool, however. Optical microscopy and quantitative analysis do not provide any data which is differentiable from the rest of the material. Though the weld is centered within the quantitative map, it is indiscernible from the surrounding material. The Zr-rich phase shown as yellow on the quantitative map extends further into the sample in this region, approximately 150 µm

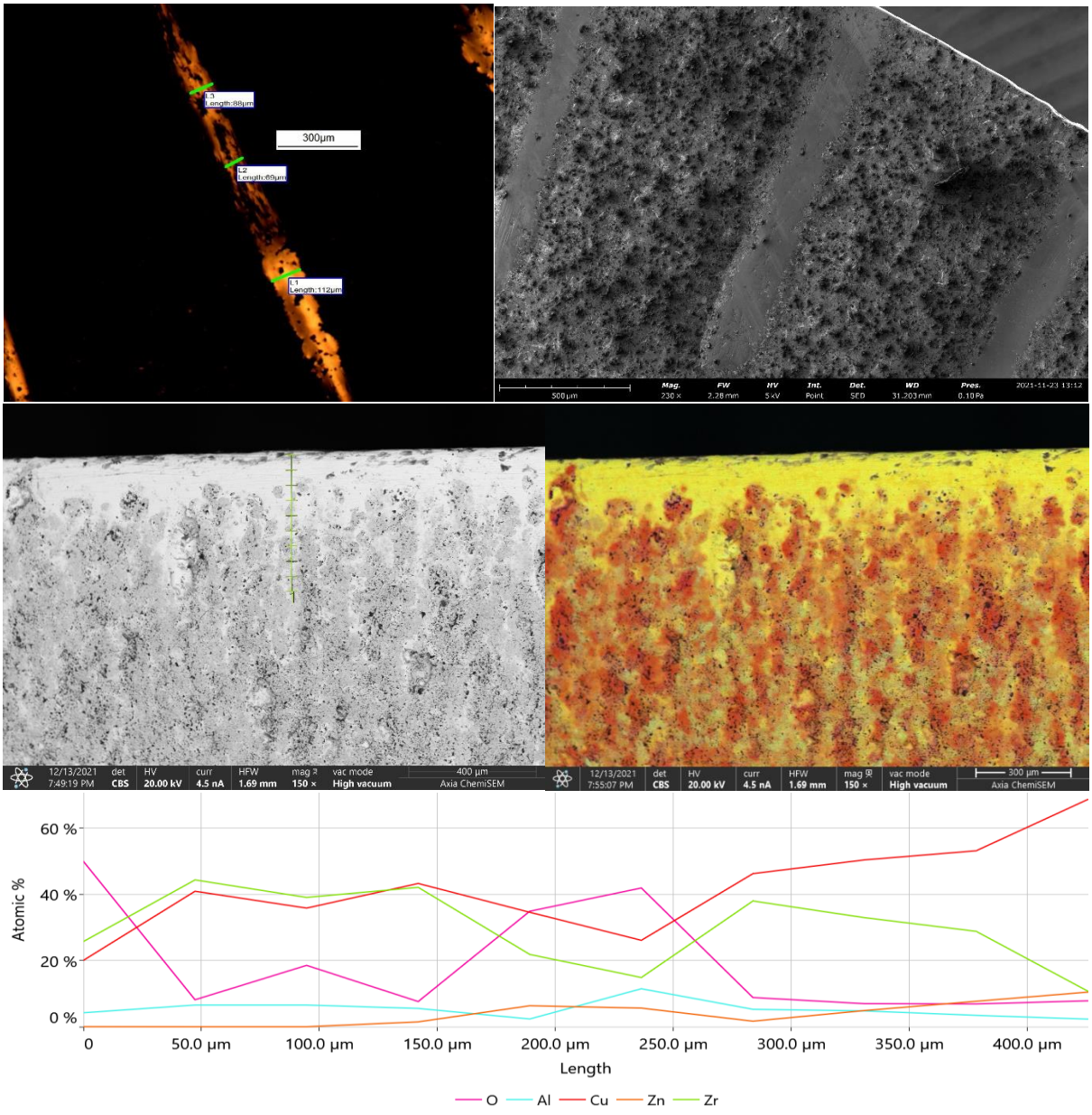

Figure 12 shows OM (top left) and SEM (top right) imagery of the weld surface, SEM imagery (center left) and a quantitative element map (center right) of the weld cross section. Compositional analysis is shown in the bottom graph.

Track 10

Figure 13 below shows OM and SEM imagery of the weld surface, SEM imagery and a quantitative map of the weld cross section, and compositional analysis of the weld. OM and SEM imagery of the weld surface show a smooth continuous phase without significant shrinkage or texturing due to volume change.

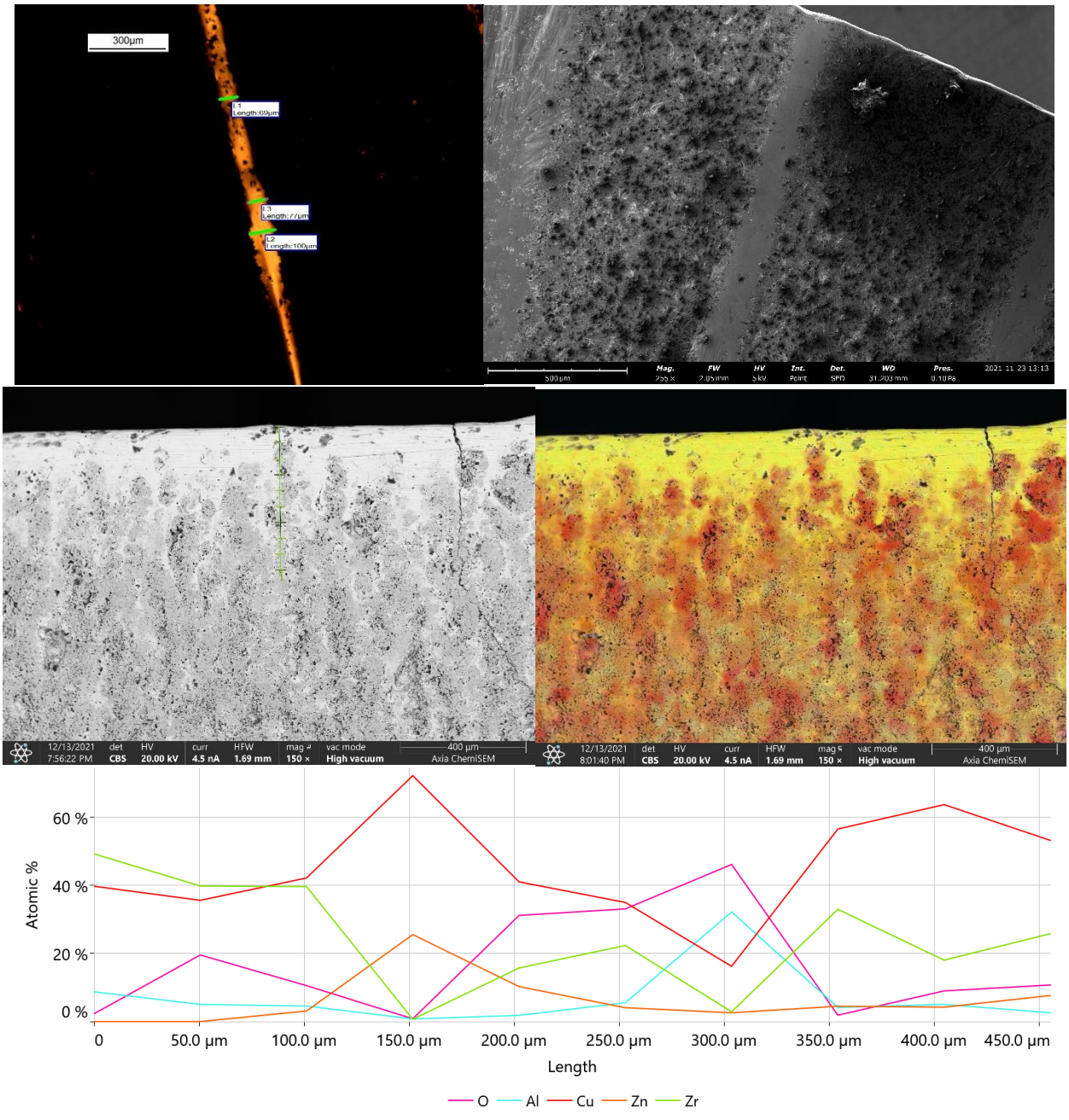

Figure 13 shows OM (top left) and SEM (top right) imagery of the weld surface, SEM imagery (center left) and a quantitative element map (center right) of the weld cross section. Compositional analysis is shown in the bottom graph.

Track 11

Figure 14 below shows OM and SEM imagery of the weld surface, SEM imagery and a quantitative map of the weld cross section, and compositional analysis of the weld. Cracks are visible on both the SEM and quantitative map of the weld cross section which match the borders of the track as labeled in OM imagery. This, coupled with the OM and SEM images of the surface showing contours parallel with the weld strongly suggest that crystallization has occurred.

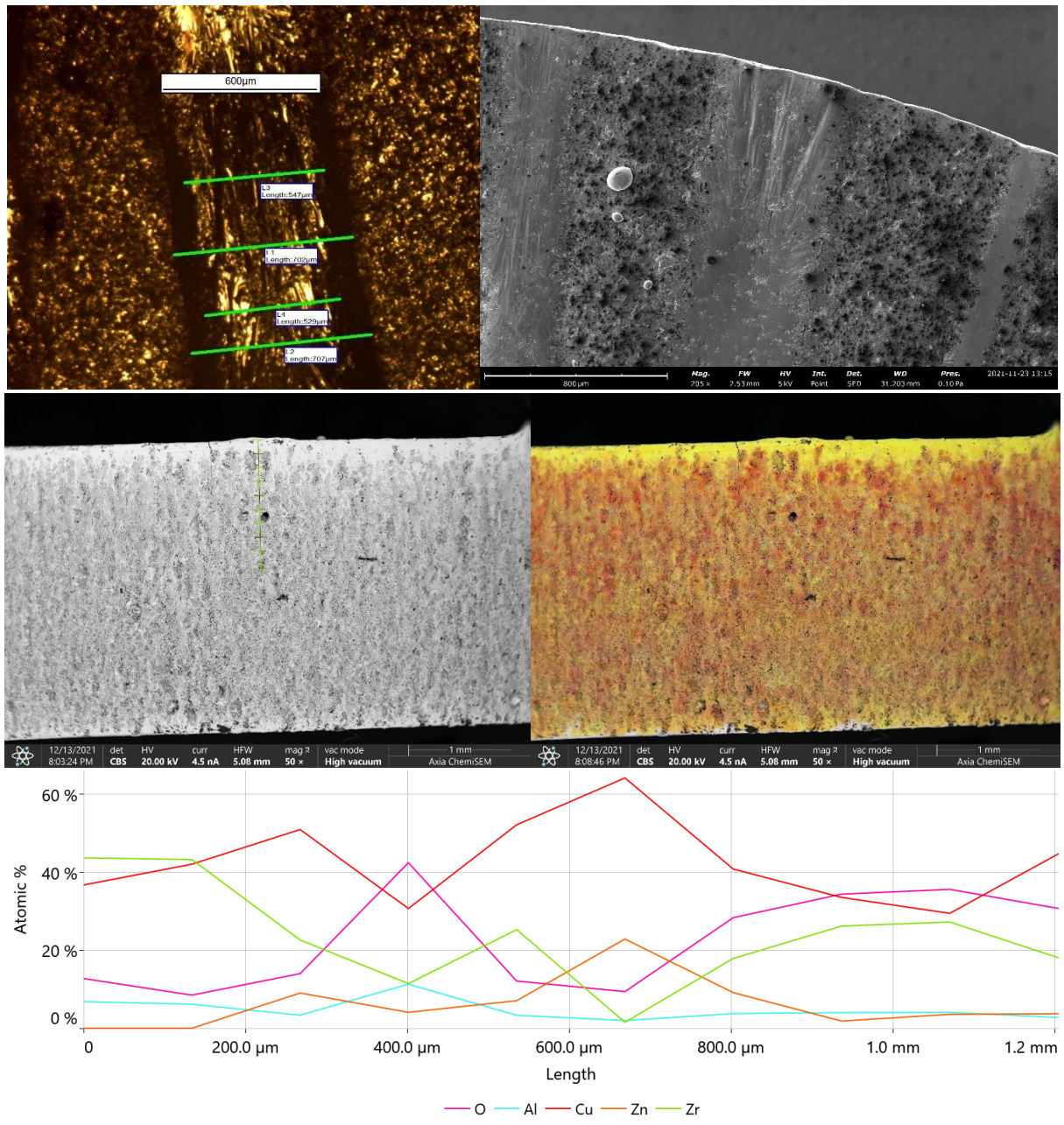

Figure 14 shows OM (top left) and SEM (top right) imagery of the weld surface, SEM imagery (center left) and a quantitative element map (center right) of the weld cross section. Compositional analysis is shown in the bottom graph.

Track 12

Figure 15 below shows OM and SEM imagery of the weld surface, SEM imagery and a quantitative map of the weld cross section, and compositional analysis of the weld. Physical contours visible in both OM and SEM imagery of the weld surface suggest significant volume changes have occurred due to crystallization. Analysis of the weld pool and HAZ through compositional analysis is difficult. Through the SEM imagery, the fusion zone appears to extend to ~175 µm, and is entirely CuZr compositionally. The HAZ appears to extend ~600 µm beneath the surface.

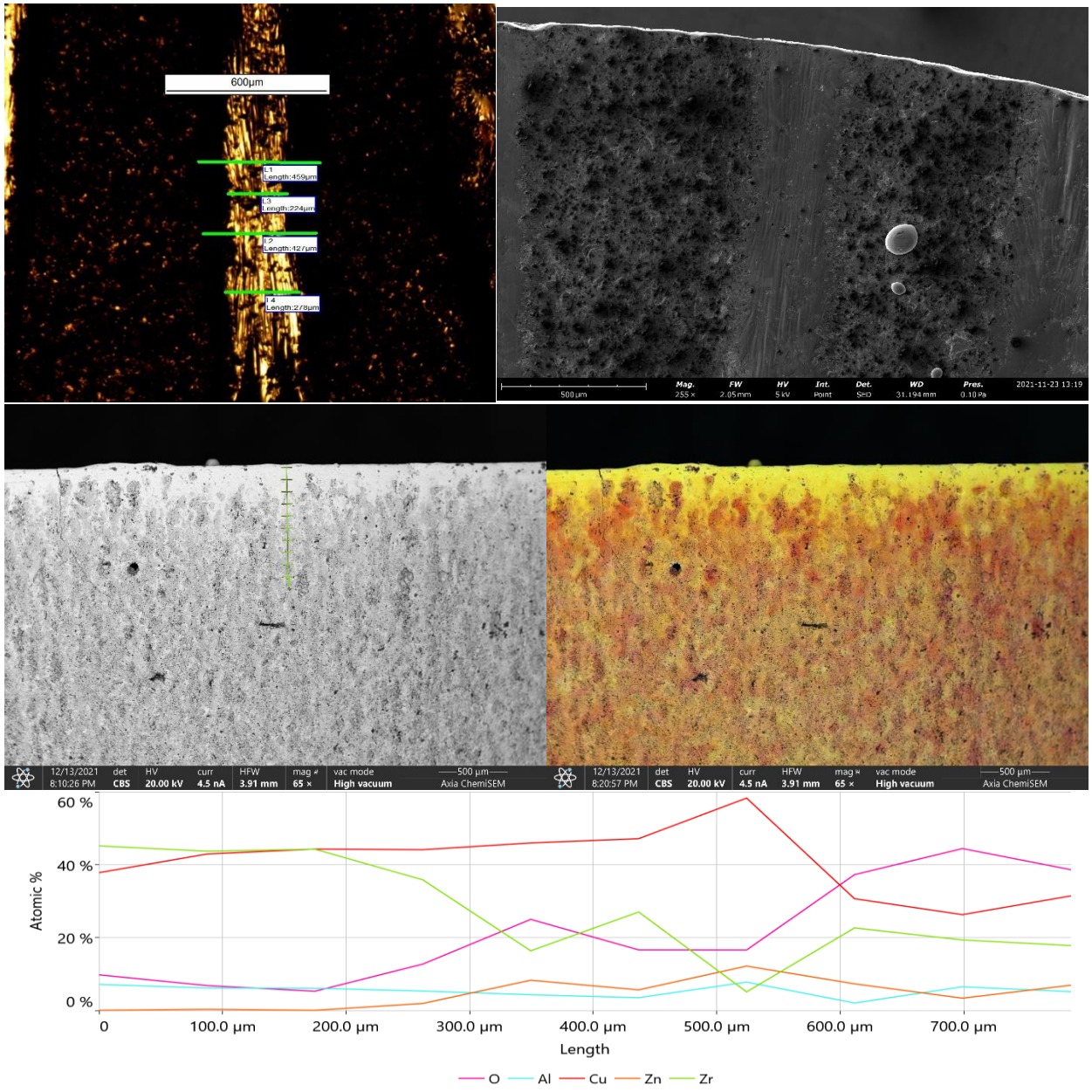

Figure 15 shows OM (top left) and SEM (top right) imagery of the weld surface, SEM imagery (center left) and a quantitative element map (center right) of the weld cross section. Compositional analysis is shown in the bottom graph.

Track 13

Figure 16 below shows OM and SEM imagery of the weld surface, SEM imagery and a quantitative map of the weld cross section, and compositional analysis of the weld. OM and SEM imagery show textures indicative of volume change. A light CuZr phase is present in the entirety of the fusion zone extending ~125 µm from the surface. Cu content remains relatively constant past that depth, with Zr decreasing significantly and fluctuating.

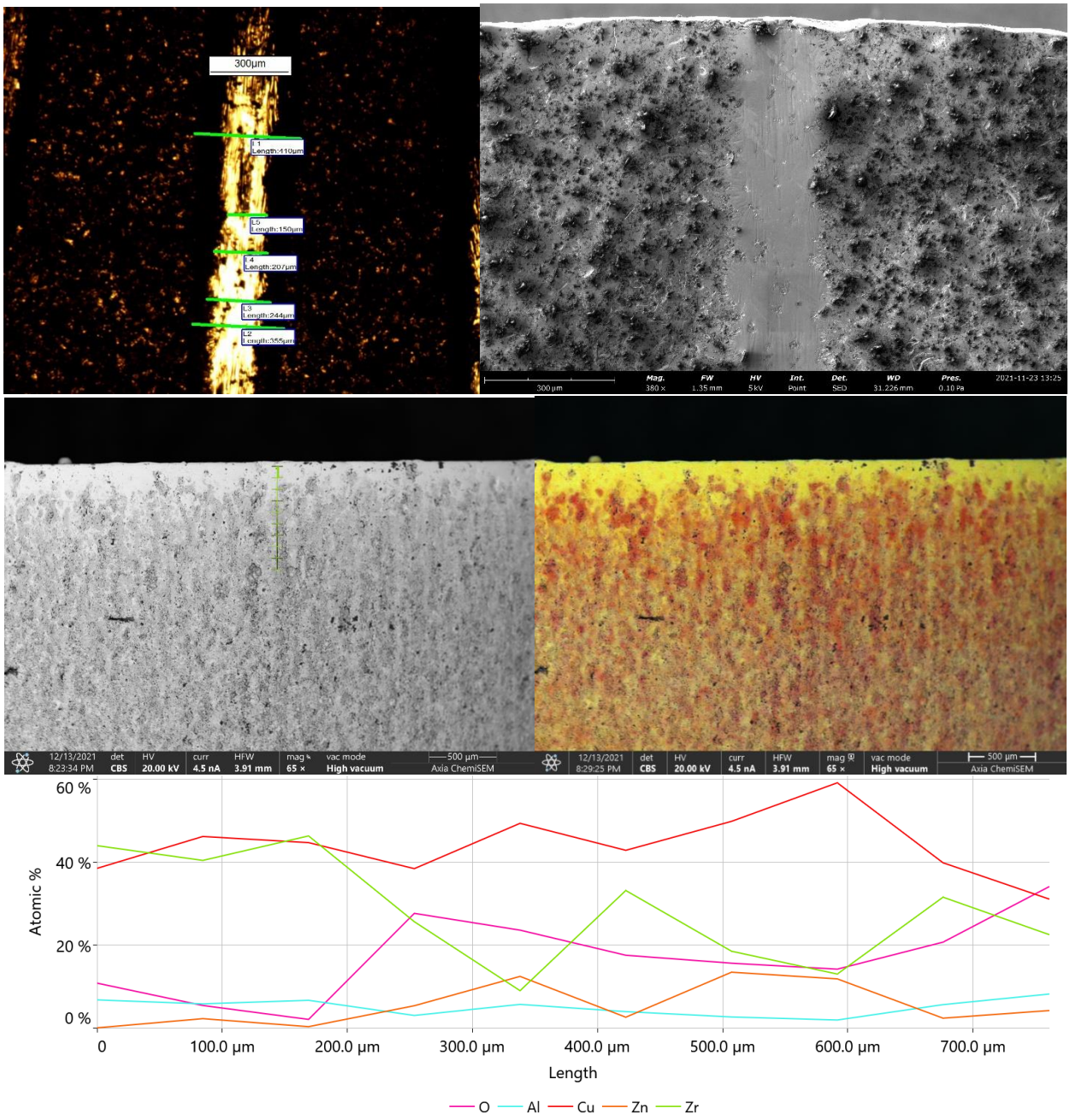

Figure 16 shows OM (top left) and SEM (top right) imagery of the weld surface, SEM imagery (center left) and a quantitative element map (center right) of the weld cross section. Compositional analysis is shown in the bottom graph.

Track 14

Figure 17 below shows OM and SEM imagery of the weld surface, SEM imagery and a quantitative map of the weld cross section, and compositional analysis of the weld. OM and SEM imagery show a textured surface indicative of large volume change. A copper rich phase (red) near the surface of the track matches the darker phase seen in SEM imagery of the weld cross section. The rapid increase of oxygen between ~500-600 µm suggests the end of the HAZ.

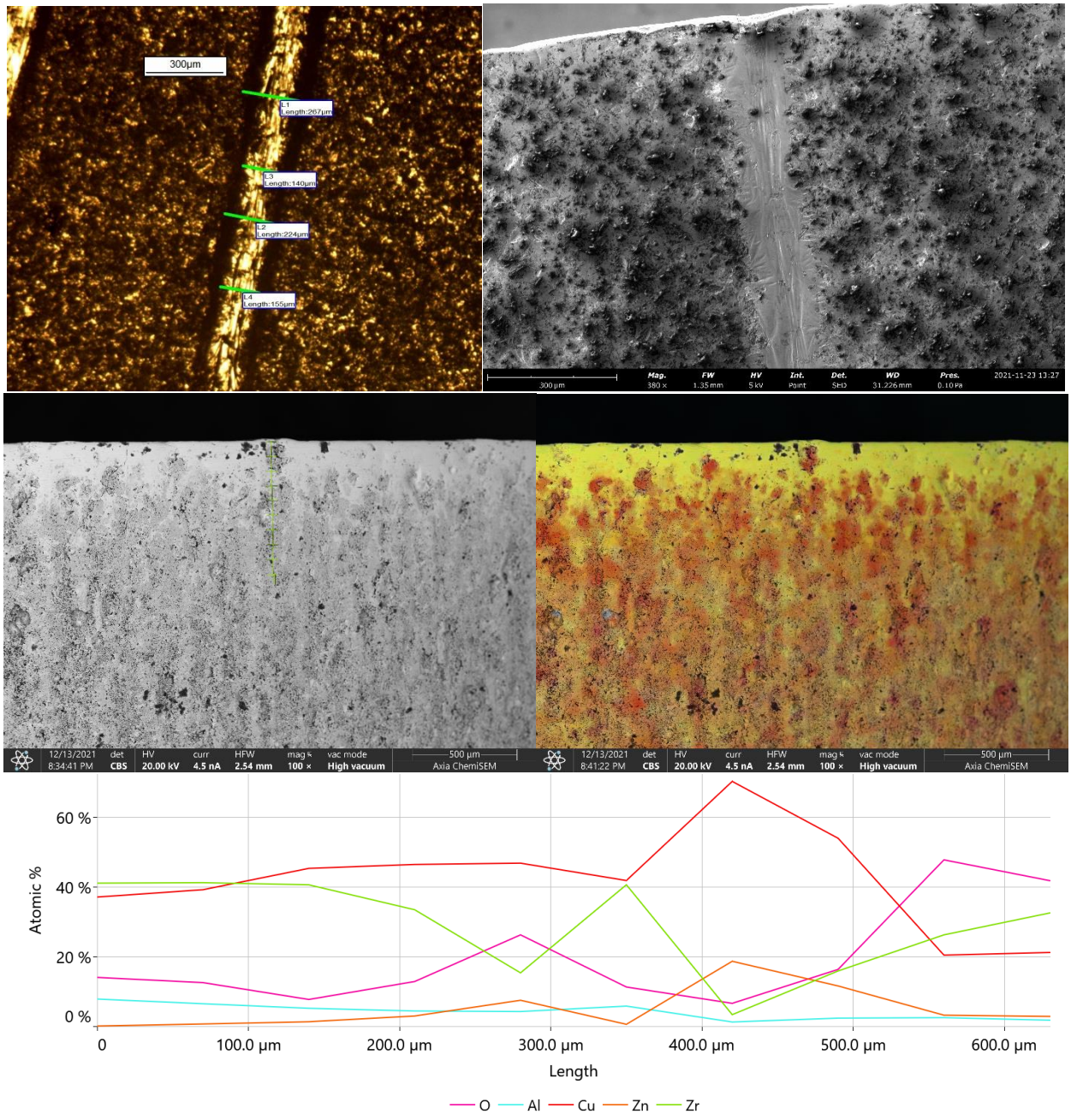

Figure 17 shows OM (top left) and SEM (top right) imagery of the weld surface, SEM imagery (center left) and a quantitative element map (center right) of the weld cross section. Compositional analysis is shown in the bottom graph.

Track 15

Figure 18 below shows OM and SEM imagery of the weld surface, SEM imagery and a quantitative map of the weld cross section, and compositional analysis of the weld. Physical texturing is present in both OM and SEM imagery of the field is present. SEM imagery of the light gray phase coincides with the equiatomic CuZr composition shown in the quantitative map. SEM imagery of the porous dark phase correlates with the more copper rich (red) phase shown in the quantitative map. Increasing oxygen content from 360-400 µm suggest the boundary between the HAZ and unaffected material.

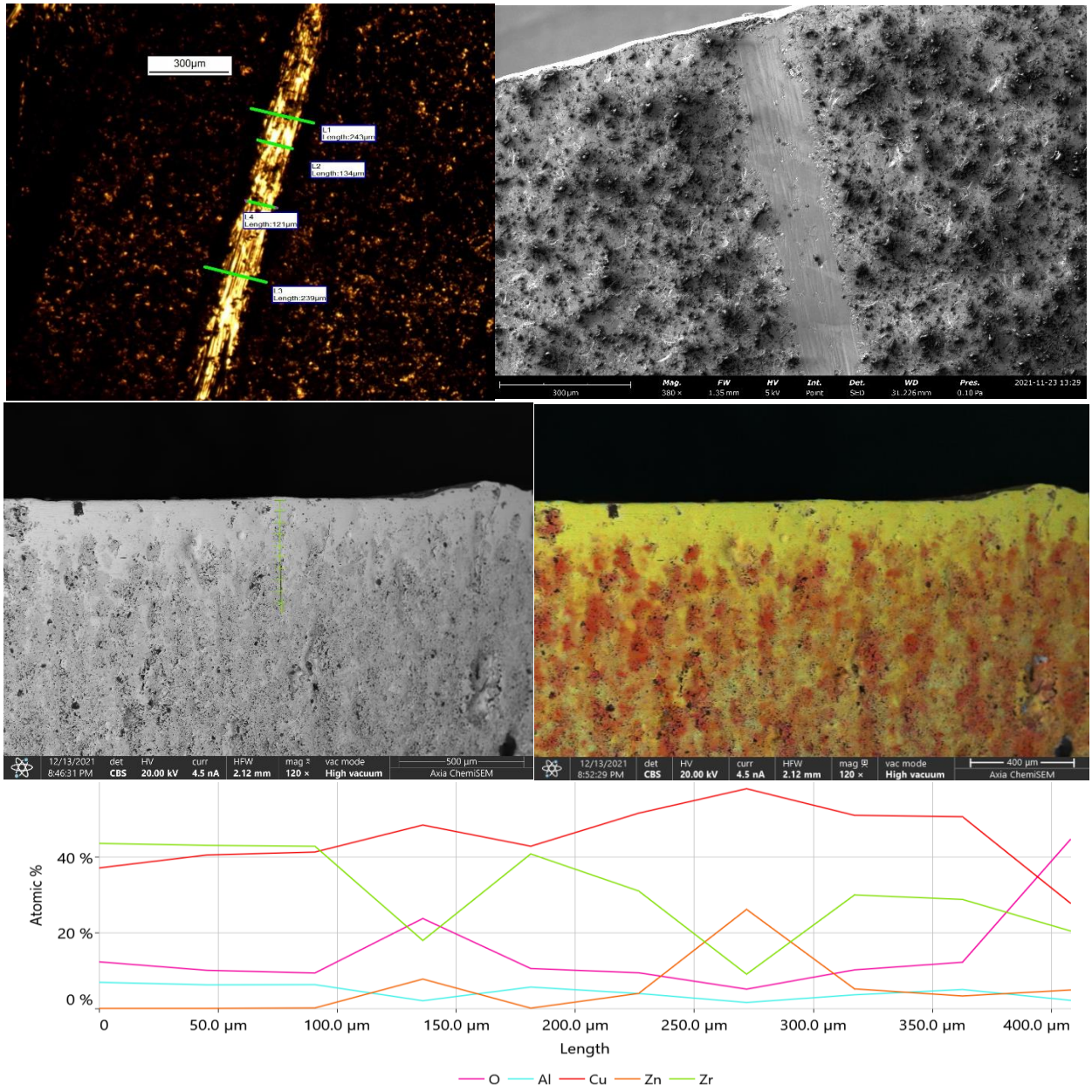

Figure 18 shows OM (top left) and SEM (top right) imagery of the weld surface, SEM imagery (center left) and a quantitative element map (center right) of the weld cross section. Compositional analysis is shown in the bottom graph.

Track 16

Figure 19 below shows OM and SEM imagery of the weld surface, SEM imagery and compositional analysis of the weld. Large amounts of physical texturing is visible in both SEM and OM imagery of the weld surface. Cracking is visible to the right of the weld in SEM imagery of the cross section. Light phase CuZr is present throughout the fusion zone, with copper content predominant throughout the entirety of the HAZ, and overall composition of the HAZ similar to that of the bulk material and appearing as a porous dark phase in optical SEM of the cross section.

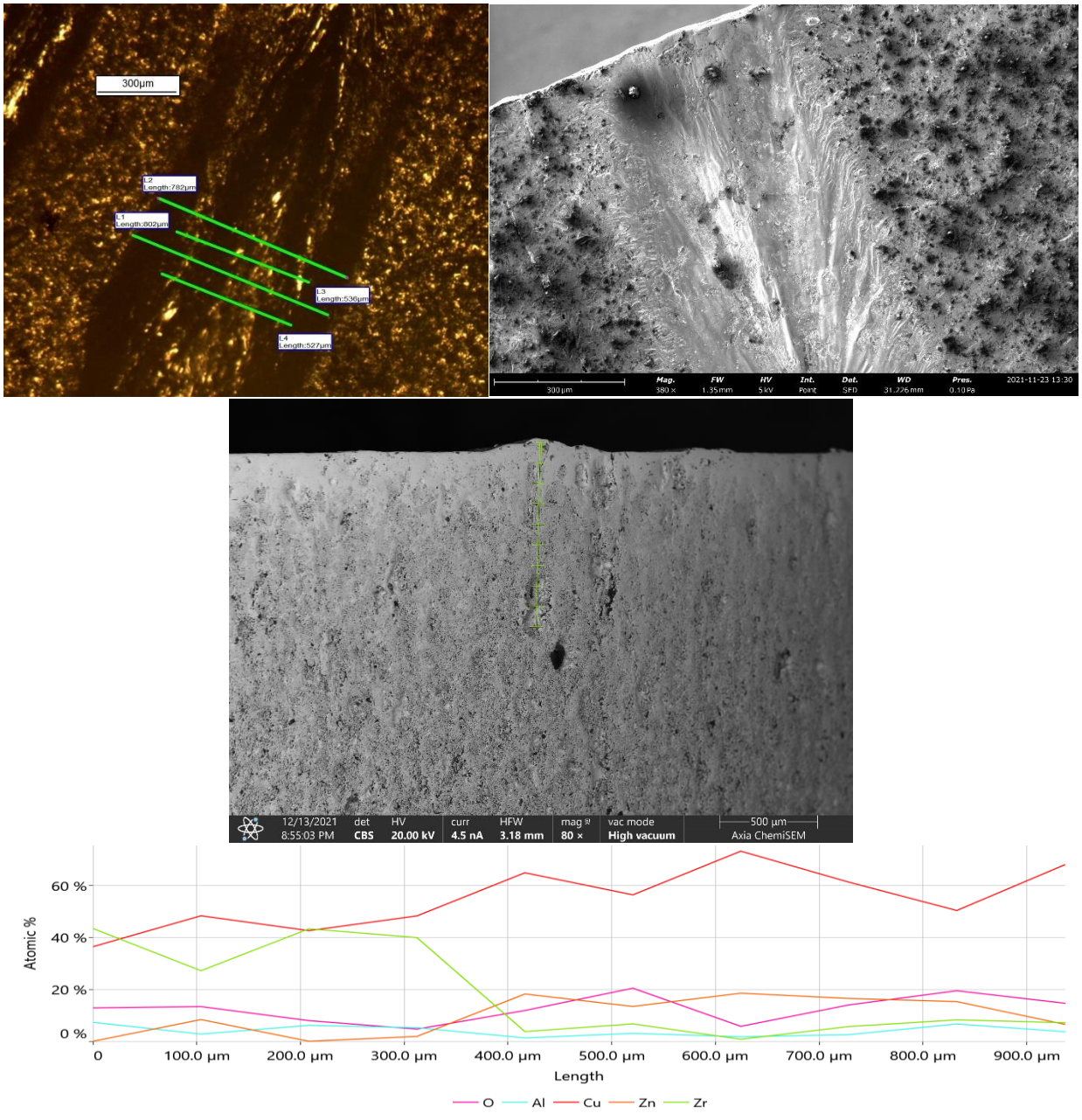

Figure 19 shows OM (top left) and SEM (top right) imagery of the weld surface, SEM imagery (center) of the weld cross section. Compositional analysis is shown in the bottom graph.

Track 17

Figure 20 below shows OM and SEM imagery of the weld surface, SEM imagery and a quantitative map of the weld cross section, and compositional analysis of the weld. OM and SEM imagery of the weld surface show a rough surface, indicative of significant volume change during cooling. SEM imagery of the cross section shows a large single phase through the weld from the surface to ~350-400 µm which. There is no cracking visible either on the surface or near the cross section of the weld.

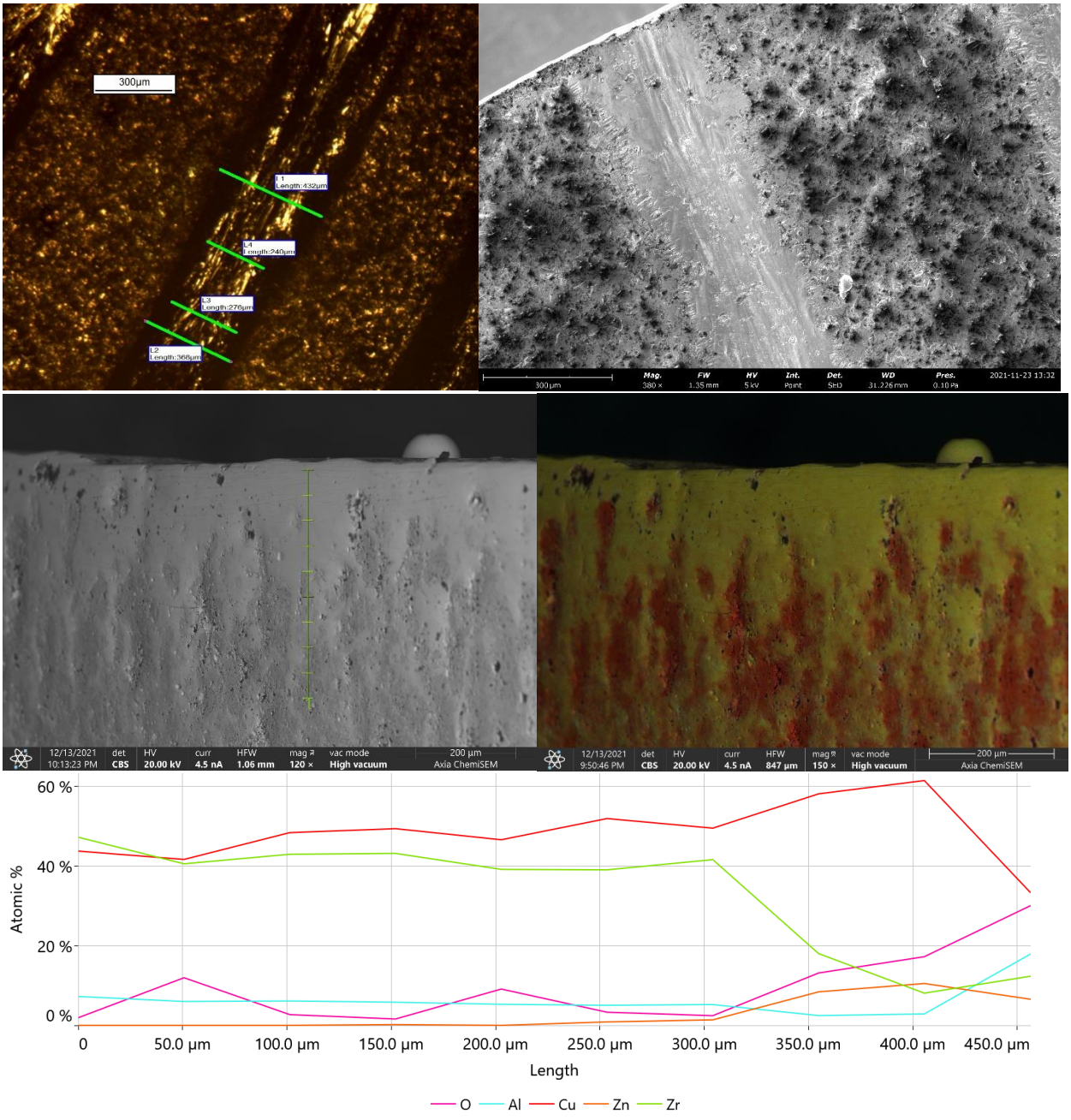

Figure 20 shows OM (top left) and SEM (top right) imagery of the weld surface, SEM imagery (center left) and a quantitative element map (center right) of the weld cross section. Compositional analysis is shown in the bottom graph.

Track 18

Figure 21 below shows OM and SEM imagery of the weld surface, SEM imagery and a quantitative map of the weld cross section, and compositional analysis of the weld. OM and SEM imagery show a rough weld surface. Compositionally, there is an increase in copper from the surface to ~200 µm, which decreases sharply to a low at ~260 µm from the surface, then gradually increases.

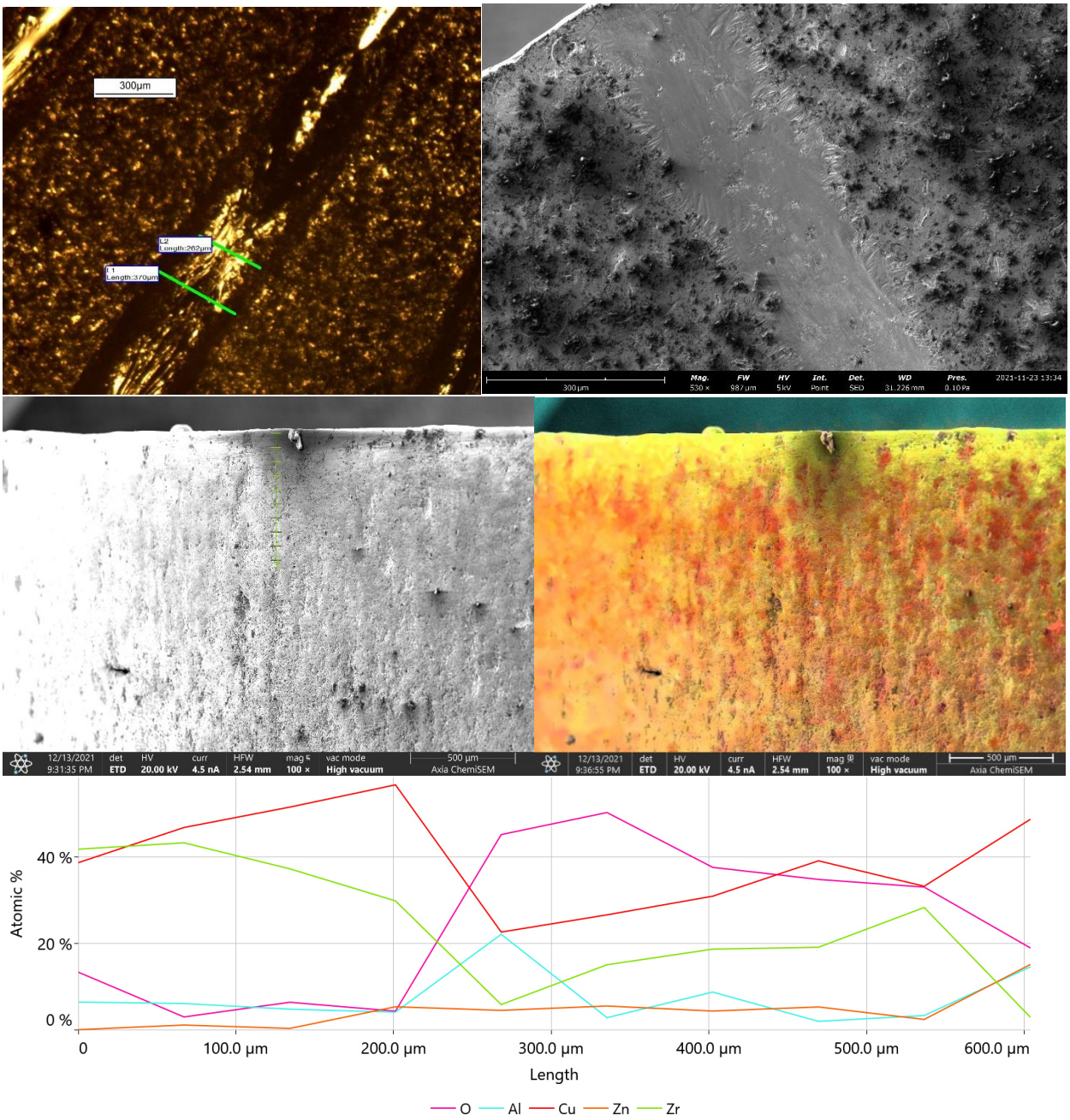

Figure 21 shows OM (top left) and SEM (top right) imagery of the weld surface, SEM imagery (center left) and a quantitative element map (center right) of the weld cross section. Compositional analysis is shown in the bottom graph.

Track 19

Figure 22 below shows OM and SEM imagery of the weld surface, SEM imagery and a quantitative map of the weld cross section, and compositional analysis of the weld. Optical microscopy shows what appears to be a very inconsistent weld pool, which is validated through SEM imagery, noting the difference in weld width between the lower right and top left of the SEM image of the surface. SEM imagery of the weld cross section shows a darker phase extending to ~175 µm within the weld corresponding to a red copper rich phase in the quantitative map, which follows the HAZ until it ends at ~235 µm below the surface.

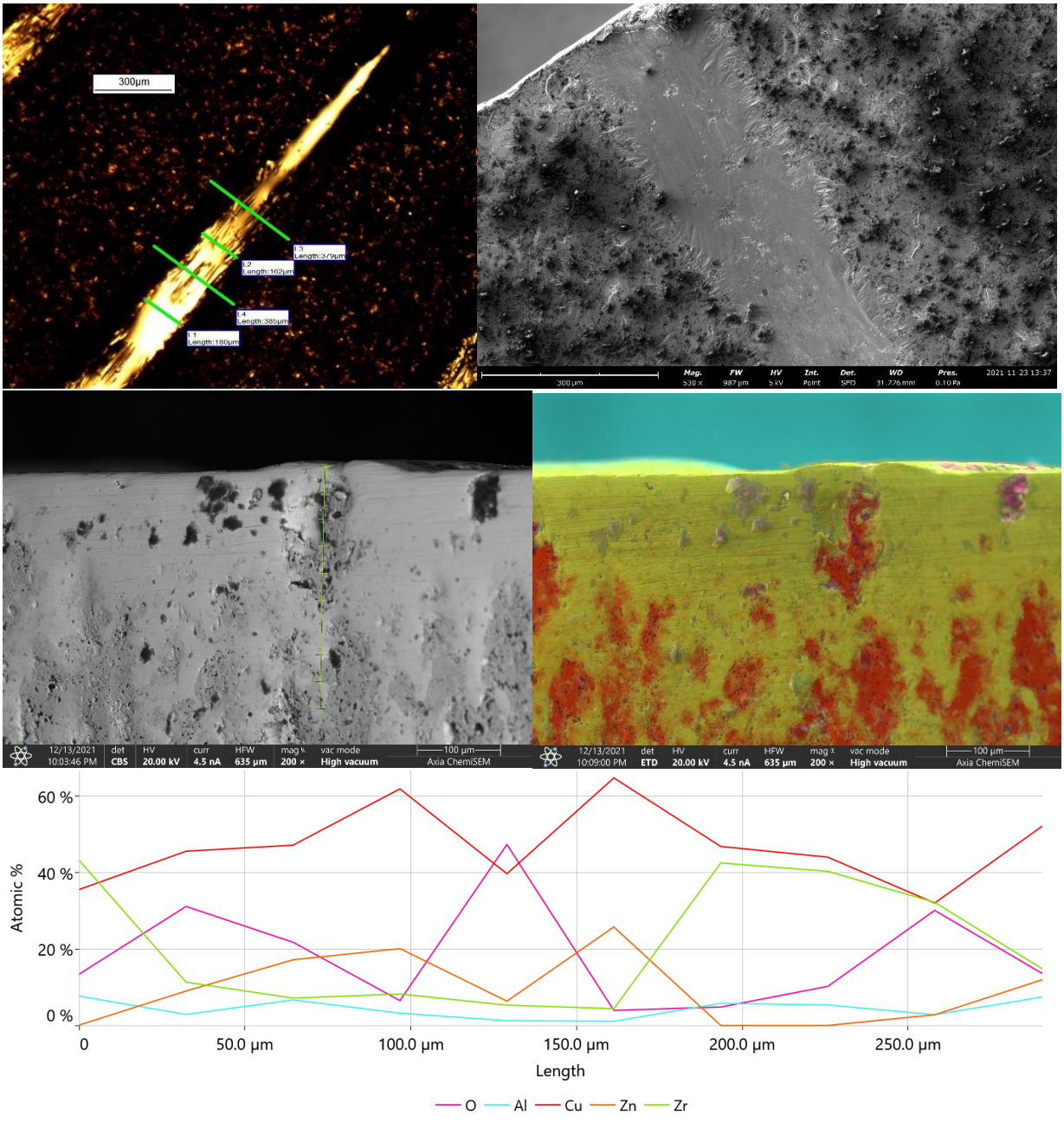

Figure 22 shows OM (top left) and SEM (top right) imagery of the weld surface, SEM imagery (center left) and a quantitative element map (center right) of the weld cross section. Compositional analysis is shown in the bottom graph.

Track 20

Figure 23 shows below shows OM and SEM imagery of the weld surface, SEM imagery and a quantitative map of the weld cross section, and compositional analysis of the weld. OM imagery shows a rough surface, which is not visible through SEM imagery of the same. SEM imagery of the weld cross section show the light CuZr phase extending to ~80 µm beneath the weld surface, with the darker Cu-rich phase present until approximately 190 µm below the surface, shown as yellow and red respectively. A subsurface crack is visible ~ 125 µm to the right of the weld

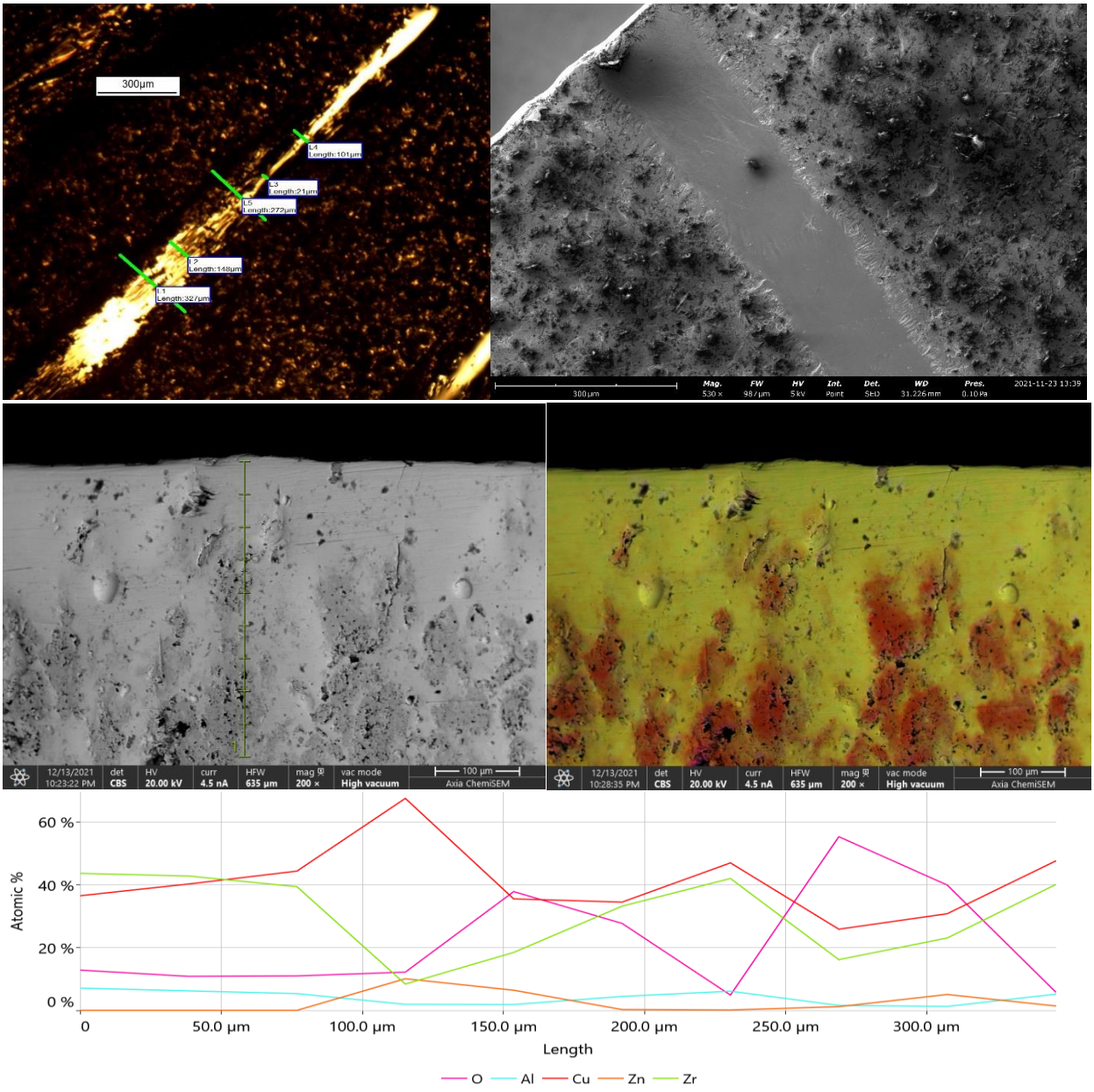

Figure 23 shows OM (top left) and SEM (top right) imagery of the weld surface, SEM imagery (center left) and a quantitative element map (center right) of the weld cross section. Compositional analysis is shown in the bottom graph.

High Power – Tracks 21 - 25

Track 21

Figure 24 below shows OM and SEM imagery of the weld surface, SEM imagery and a quantitative map of the weld cross section, and compositional analysis of the weld. A rough surface is visible in both OM and SEM imagery of the weld surface, with lighter and darker phases present within the fusion zone. The fusion zone extends to 150 µm below the surface and is predominantly CuZr, with a dark Cu-rich phase also present. A crack is visible through the weld pool and to the right of the weld. After 250 µm there is no differentiation in composition between the HAZ and base material due to large variances in Cu, Zr, and O content

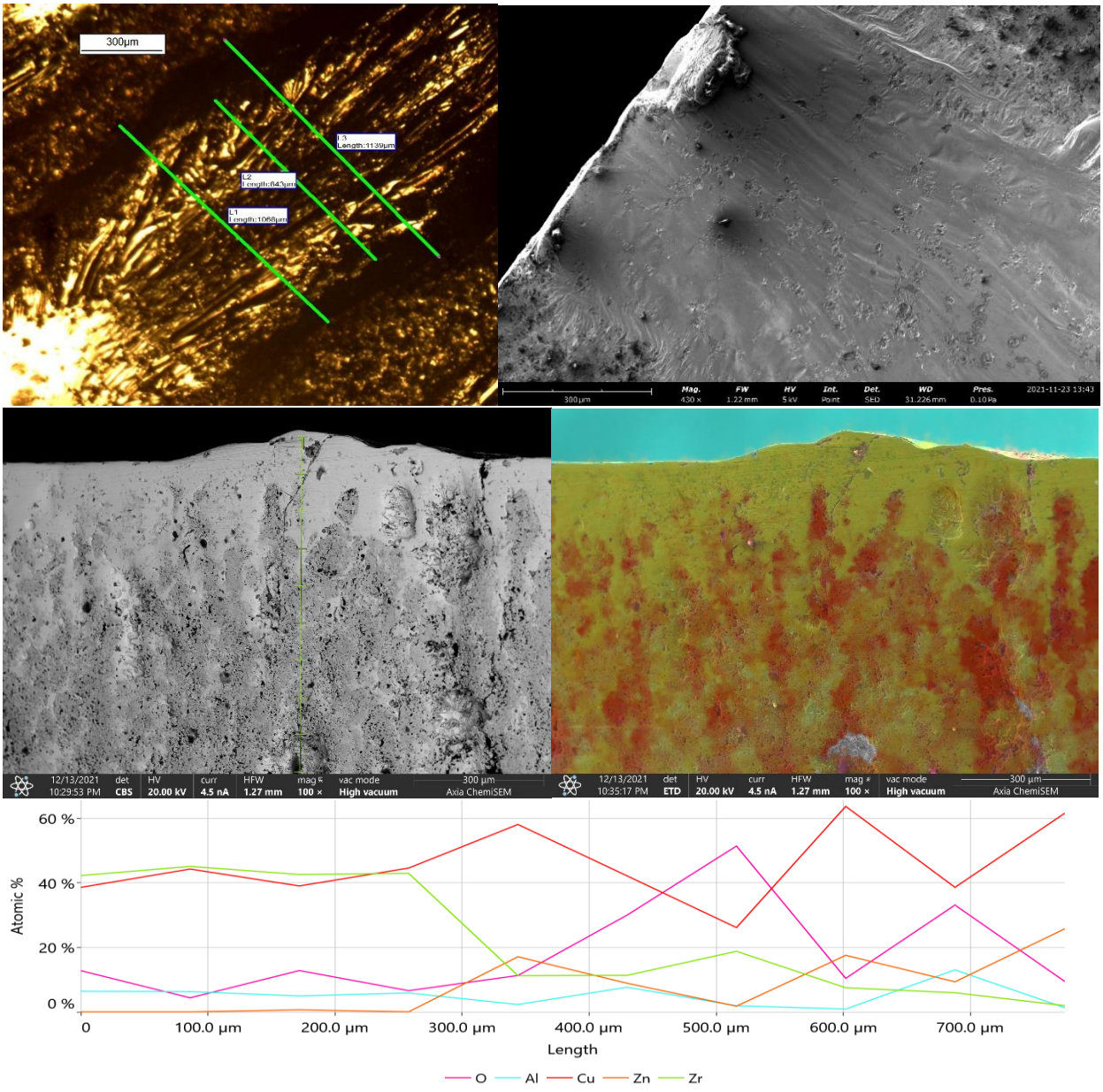

Figure 24 shows OM (top left) and SEM (top right) imagery of the weld surface, SEM imagery (center left) and a quantitative element map (center right) of the weld cross section. Compositional analysis is shown in the bottom graph.

Track 22

Figure 25 below shows OM and SEM imagery of the weld surface, SEM imagery and a quantitative map of the weld cross section, and compositional analysis of the weld.

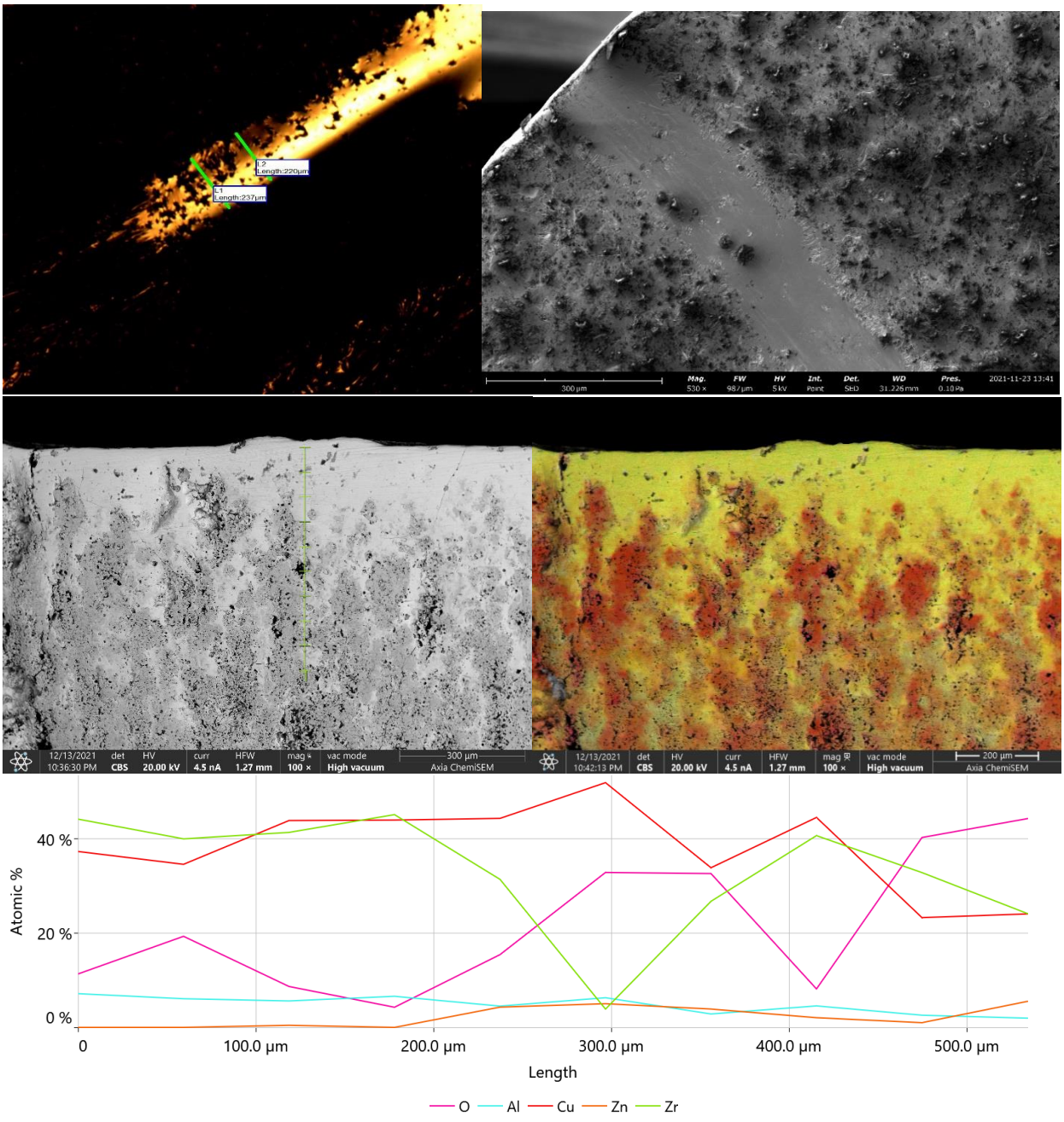

Figure 25 shows OM (top left) and SEM (top right) imagery of the weld surface, SEM imagery (center left) and a quantitative element map (center right) of the weld cross section. Compositional analysis is shown in the bottom graph.

Track 23

Figure 26 below shows OM and SEM imagery of the weld surface, SEM imagery and a quantitative map of the weld cross section, and compositional analysis of the weld. The weld

surface appears smooth and mostly continuous in both OM and SEM imagery. The CuZr phase extends from the surface to ~250 µm, and darker Cu-rich phase inclusions. Cracks are visible both to the left and right of the weld.

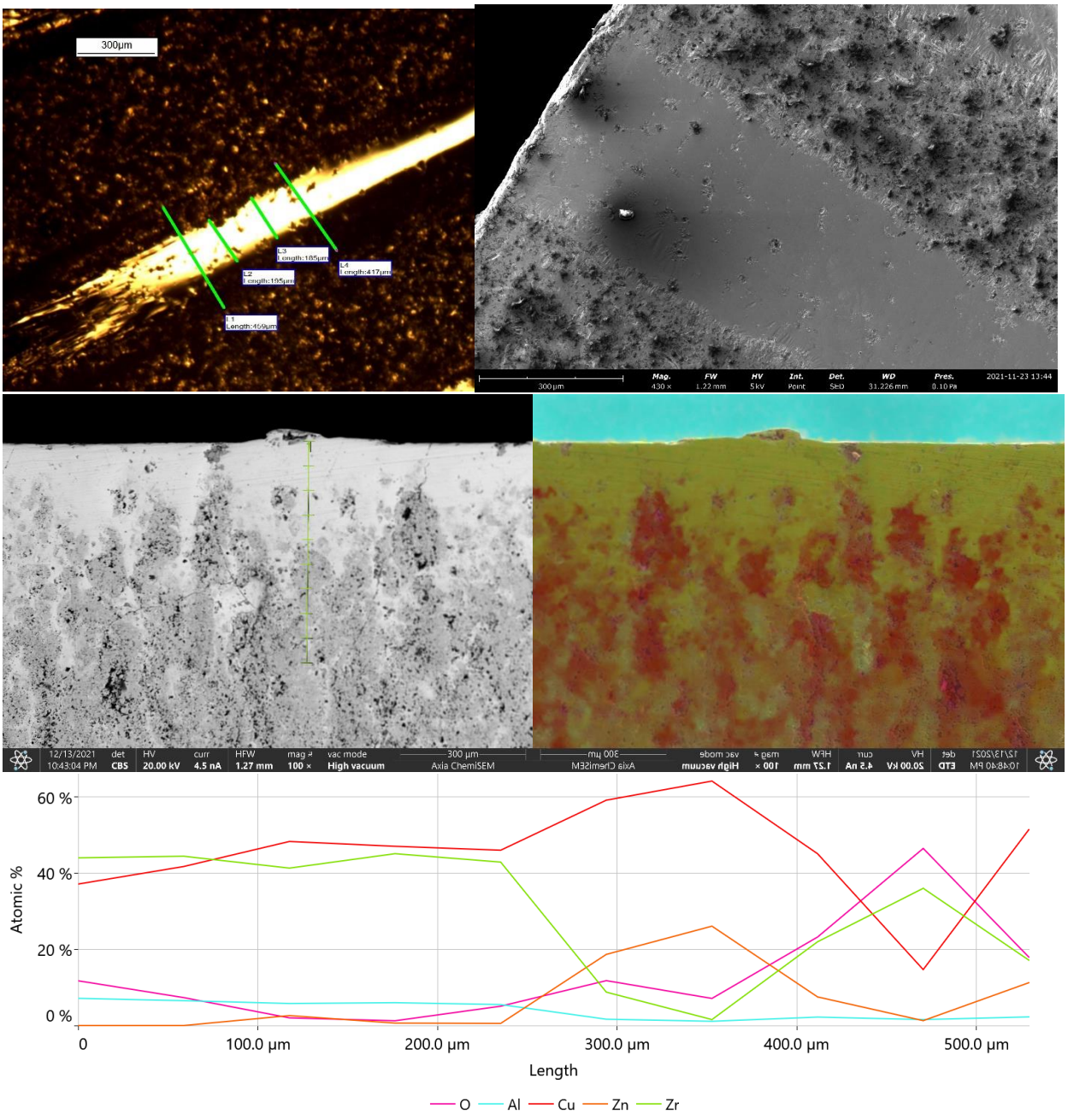

Figure 26 shows OM (top left) and SEM (top right) imagery of the weld surface, SEM imagery (center left) and a quantitative element map (center right) of the weld cross section. Compositional analysis is shown in the bottom graph.

Track 24

Figure 27 below shows OM and SEM imagery of the weld surface, SEM imagery and a quantitative map of the weld cross section, and compositional analysis of the weld. OM and SEM imagery show a continuous but pitted surface with single phase present along the surface.

SEM imagery of the cross section shows a crack to the right of the weld. Compositional analysis shows a light CuZr phase extending to ~160 µm below the surface, with dark Cu rich phase extending further into the material. Cracks are visible to the right of the weld in the cross sectional SEM imagery.

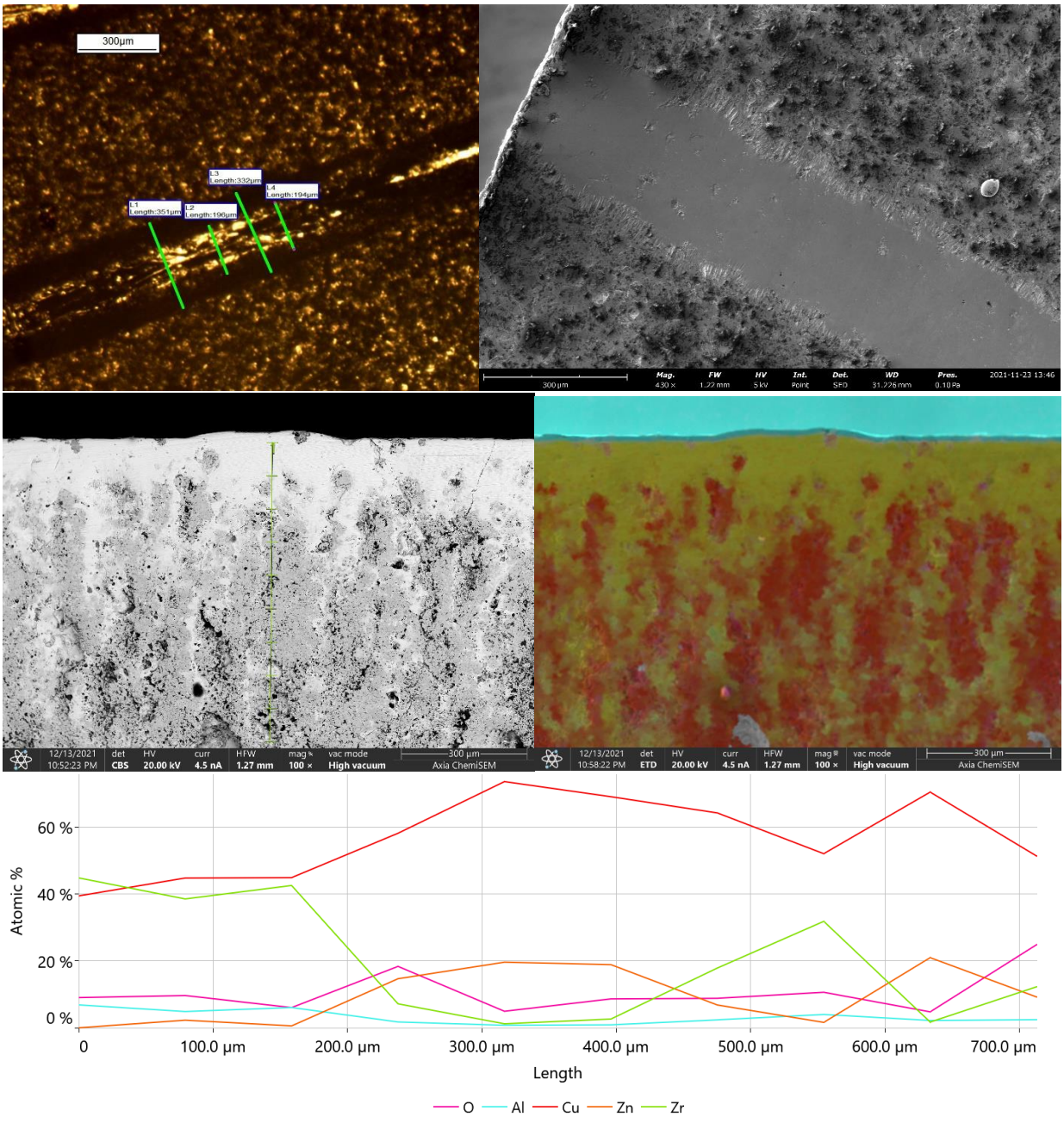

Figure 27 shows OM (top left) and SEM (top right) imagery of the weld surface, SEM imagery (center left) and a quantitative element map (center right) of the weld cross section. Compositional analysis is shown in the bottom graph.

Track 25

Figure 28 below shows OM and SEM imagery of the weld surface, SEM imagery and a quantitative map of the weld cross section, and compositional analysis of the weld. OM and

SEM imagery of the weld surface show a rough surface. Quantitative analysis shows a CuZr phase extending from the surface to 100 µm below the surface. Quantitative mapping shows what appears to be fibrils of CuZr extending along the

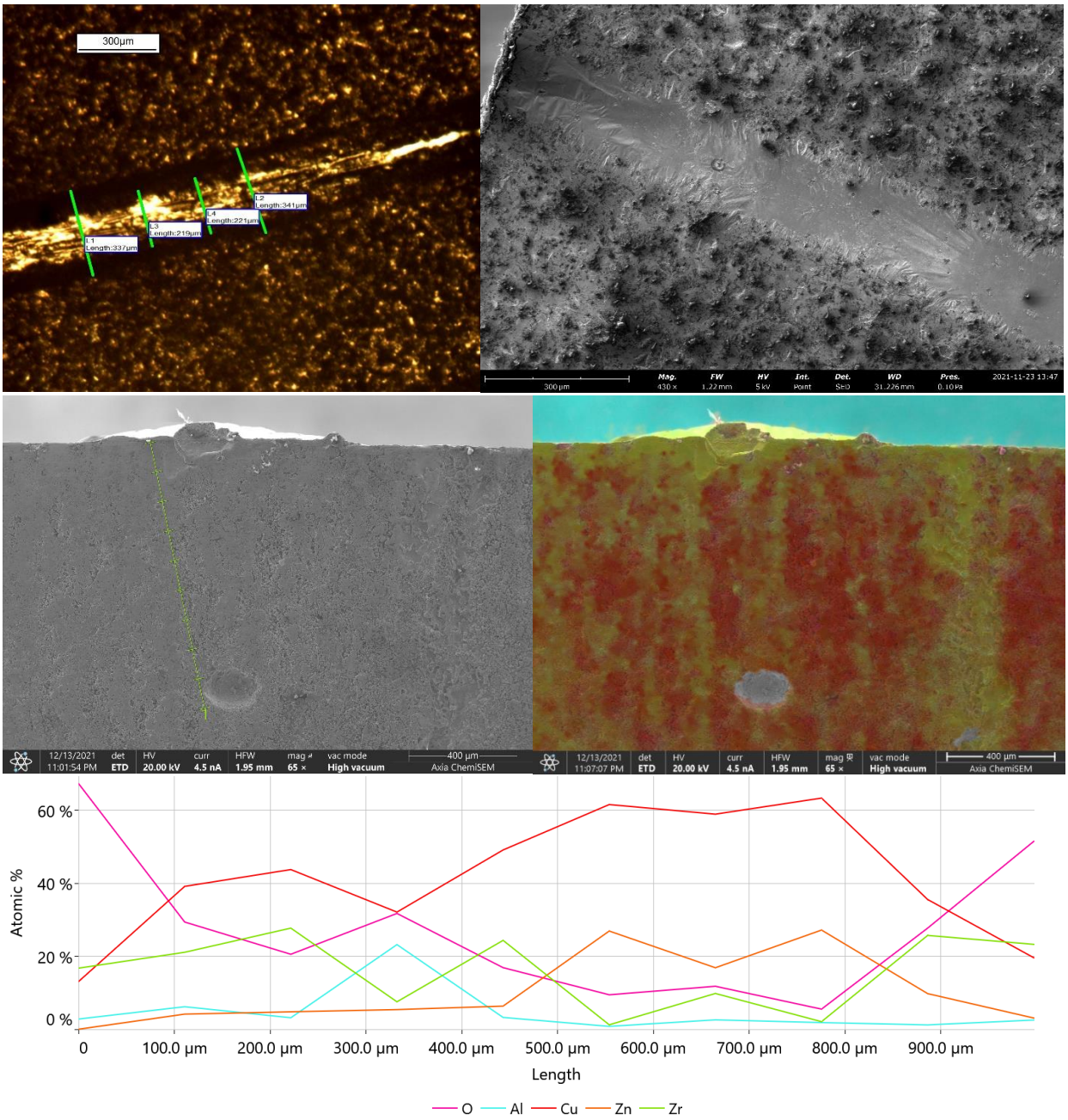

Figure 28 shows OM (top left) and SEM (top right) imagery of the weld surface, SEM imagery (center left) and a quantitative element map (center right) of the weld cross section. Compositional analysis is shown in the bottom graph.

Discussion

Low Power, 75W, Tracks 1-5

The welds created at laser power levels below what has been established as optimal in literature, differentiation of the weld from the base material is difficult from the base material. The welds are smaller physically, and experience negligible, if any, compositional changes from the base material. It was noted that Cu content increases through the fusion zone and decreases through the HAZ (Figures 3-8, bottom), then returns to levels similar to the unprocessed base material (Figure 2, bottom). Optical and SEM imagery of the weld surfaces (Figures 3-8, top left and top right) show discontinuous, irregular weld tracks which are expected due to the lack of molten material formed at low laser power levels. Inadequate laser power for processing corresponds to inadequate amounts of material which is melted. Welds became smoother but more irregular as energy density levels found in tracks 4 and 5 of 0.08 J/mm and 0.11 J/mm (Figures 7 and 8, top left and right) varying both in weld width and shape.

Moderate Power, 150-300W

The welds created at laser power levels within the optimal power range varied in size and continuity which was dependent on energy density. With the exception of tracks 13, 17, and 22, copper content increased through the fusion zone. A continuous CuZr phase forms across the surface of the material beginning between tracks 5 and 6 (Figure 7) for various possible reasons and extended through the rest of the welds. Cross sectional weld features were more easily identifiable at tracks 17 and 19, but at energy densities above 0.75 J/mm, differentiation of the HAZ from the base material is difficult if cracks are not present which border the weld. Additionally, compositional changes within this region, notably the fibrils of the lighter CuZr phase within this region which extend perpendicular and away from the surface make weld feature identification more difficult, both through SEM and quantitative analysis. It may be true that this change in composition and microstructural structure of the phases present support current literature, however without analysis of phase morphology, it cannot be determined definitively what is crystalline and what is not. Cracking is present in tracks 11 and 16, visible in Figures 13 and 18, center left and right. Linear energy densities of tracks 11 and 16 were 2.25 and 3 J/mm respectively, this combined with the cracking creates an apparent upper limit for processing the material at these power levels. The depth of the CuZr phase increased with laser power, which if it were crystalline would suggest possible errors in processing due to the 1.5mm weld spacing.

High Power, 370W, Tracks 21-25

Welds created at laser power levels above the optimal power range for processing experienced large amounts of cracking, fusion zones entirely of the light CuZr phase, irregular surfaces, and long CuZr fibrils extending beneath the sample. Linear energy densities varied from 3.7 J/mm at Track 21, to 0.41 J/mm at track 25. Cu content increased through the fusion zones of all the tracks. Though energy densities below 0.75 J/mm at moderate power levels provided welds which did not experience cracking and provided a clear weld, this trend does not remain at high power levels.

Sources of Error

There are several factors which have been found that affect the quality of the data gathered. First, the wire EDM cutting of the sample did not yield a flat surface, this made cross-sectional imagery and analysis more difficult. Second, the unexplained presence of Zinc in significant amounts in the base material and all weld tracks affected the relative at.% of other phases, making phase identification difficult, and compositional analysis more challenging. Proper identification of phases is crucial in compositional analysis. Adequate quantitative mapping is also important. Tracks which did not have associated quantitative maps included are also more difficult to visually analyze for compositional changes through the material.

Conclusions

At and above a critical laser power between 75-100 W, a CuZr phase forms on and around welds. Cu content increases from the surface to the edge of the fusion zone, and drops significantly as the heat affected zone is entered at low and moderate laser power levels. Within the established processing parameters, fibrils of light CuZr phase form at the surface and penetrate into the material. From this experiment cracking appears to be more dependent on power level than on energy density, supporting Bertoli's conclusion in his paper that Energy Density alone is inadequate in predicting additive manufacturing processing parameters. Further research is needed to determine morphology, %crystallinity, and boundaries of the welds.

Bibliography

Junwei, Q., Haoling, J. Liaw, P. “Metallic glass matrix composites” Materials Science and Engineering R, 2016, pp. 1-69.

Trexler, M., and Thadhani, N. “Mechanical Properties of Bulk Metallic Glasses.” Progress in Materials Science, vol. 55, no. 8, 2010, pp. 759–839.

Cheng, Y.Q., and Ma, E. “Atomic-Level Structure and Structure-Property Relationship in Metallic Glasses.” Progress in Materials Science, vol. 56, no. 4, 2010, pp. 379–473.

Lin, X, and Johnson. “Formation of Ti–Zr–Cu–Ni Bulk Metallic Glasses.” Journal of Applied Physics, vol. 78, no. 11, 1998, pp. 6514–6519.

Klement, W., Willens, R.H., Duwez, P. “Non-crystalline Structure in Solidified Gold-Silicon Alloys” Nature Vol. 187, 1960, pp. 869-870

Wu, Wenzheng, et al. “Ultrasonic Additive Manufacturing of Bulk Ni-Based Metallic Glass.” Journal of Non-Crystalline Solids, vol. 506, 2019, pp. 1–5.

Liebermann, H., and Graham, Jr.,C. “Production of Amorphous Alloy Ribbons and Effects of Apparatus Parameters on Ribbon Dimensions” IEEE Transactions on Magnetics, Vol. MAG-12, No. 6, Nov. 1976, pp. 921-923

Li, Yingqi, et al. “Mechanical Properties of Zr-Based Bulk Metallic Glass Parts Fabricated by Laser-Foil-Printing Additive Manufacturing.” Materials Science & Engineering A, vol. 743, 2019, pp. 404–411.

Bordeenithikasem, Punnathat, et al. “Enhanced Mechanical Properties of Additively Manufactured Bulk Metallic Glasses Produced through Laser Foil Printing from Continuous Sheetmetal Feedstock.” Additive Manufacturing, vol. 19, no. C, 2017, pp. 95–103.

Bordeenithikasem, Punnathat, et al. “Glass Forming Ability, Flexural Strength, and Wear Properties of Additively Manufactured Zr-Based Bulk Metallic Glasses Produced through Laser Powder Bed Fusion.” Additive Manufacturing, vol. 21, 2018, pp. 312–317.

Bordeenithikasem, Punnathat, et al. “Controlling microstructure of FeCrMoBC amorphous metal matrix composites via laser directed energy deposition” Journal of Alloys and Compounds 857 (2020) 157537

Hofmann, Douglas, et al. “Developing Processing Parameters and Characterising Microstructure and Properties of an Additively Manufactured FeCrMoBC Metallic Glass Forming Alloy” Advanced Engineering Materials: 2018, 1800433

Bertoli, Umberto, et al. “On the limitations of Volumetric Energy Density as a design parameter for Selective Laser Melting” Materials and Design, 2016 pp. 331-340

Mohandas, T, et al. “Heat-Affected Zone Softening in High-Strength Low-Alloy Steels.” *Journal of Materials Processing Technology*, vol. 88, no. 1-3, 1999, pp. 284–294., https://doi.org/10.1016/s0924-0136(98)00404-x.

Li X.P. et al. “Selective Laser Melting of Zr-Based bulk metallic glasses: Processing, microstructure and mechanical poperties” Materials and Design (2006) pp. 217-226

Ouyang et al. “3D printing of crack-free high strength Zr-based bulk metallic glass composite by selective laser melting” Intermetallics 90 (2017) pp. 128-134